6   Practical Exact-Constraint Design

The basic concepts of kinematics and exact-constraint design are presented in Section 2.6 following the 12 statements from [Blanding, 1992]. This chapter brings those concepts closer to reality by considering various constraint devices and the many ways that constraints may be arranged. Several analytical studies on flexures provide deeper understanding into the particulars of flexure design. A new approach for kinematic-coupling design optimizes the ability of the coupling to overcome friction and become centered. The approach is most useful for unusual, nonsymmetric configurations where intuition is inadequate. The sometimes complex spatial relationships between constraints, whether for flexures or in couplings, soon become insurmountable unless systematic, matrix-algebra techniques are used to manage all the terms. Working through many such problems has culminated in generalized kinematic modeling software. Written in Mathcad™ Plus 6, programs for flexure systems and kinematic couplings appear in Section 6.1.

6.1 Useful Constraint Devices and Arrangements

Kinematic devices serve many applications that generally require one or more of the following features: 1) separation and repeatable engagement as with a kinematic coupling, 2) defined motion along or about one or more axes, and 3) minimum influence that an imprecise or unstable foundation has on the elastic stability of a precision component. A device is kinematic if it provides the proper number of constraints required for the intended purpose. For example, a supported object should have $n = 6 + f - d$ independent constraints to exactly constrain six rigid-body degrees of freedom plus f flexural degrees of freedom minus d desired axes of motion. In addition to the proper number of constraints, a kinematic design is free of overconstraint.

A purely kinematic design may be difficult (or expensive) to achieve in practice. The term *semi-kinematic* has been used to describe designs that are impure to some extent. That should not imply something is wrong; rather, there are tradeoffs to make in almost every design. It is important to understand the advantages and limitations of various constraint types so tradeoffs can be made to best satisfy the application. I strictly avoid classifying designs as kinematic, semi-kinematic or non-kinematic because there will always be ambiguity. Instead, I advocate applying kinematic design principles within the limits of practical constraint devices; there will almost always be some benefit in doing so. This approach is not limited to precision design but applies to more general machine and mechanism design. See, for example, [Kamm, 1990] and [Reshetov, 1982].

The constraint devices common to precision applications tend to fall into three categories: 1) relatively short-travel flexural bearings (e.g., blade flexures), 2) relatively long-travel bearing components, and 3) repeatable connect-disconnect couplings (e.g.,

kinematic couplings). This chapter focuses on blade flexures and kinematic couplings. Chapter 8, *Anti-Backlash Transmission Design*, presents several common bearing components. See [Slocum, 1992] for more extensive treatment of bearing components.

6.1.1 Basic Blade Flexures

This section presents several common arrangements of blade flexures that provide one axis of motion over a short range of travel. These arrangements: parallel blades, cross blades, and axial blades, are well documented in the literature perhaps with slightly varying names. See, for example, [Jones, 1951, 1962], [Weinstein, 1965], [Siddall, 1970], [Vukobratovich and Richard, 1988] and [Smith, 1998]. A key concept to learn from this section is summarized in the following statement. Several blades connected together as parallel constraints (as opposed to serial constraints) will retain the degrees of freedom that the individual blades have in common. This concept will become clearer after examining the arrangements in this section.

Two parallel blades, connected as shown in Figure 6-1, share a common translational degree of freedom. The rotational degrees of freedom of the individual blades occur about axes that are not in common, thus the combination of two blades constrains those degrees of freedom. Both blades redundantly constrain rotation about the translational axis. A displacement δ_z in the direction of freedom has an associated second-order displacement δ_x given by Equation 6.1. This behavior is a general concern for all flexure designs. All other constraint directions have nominally zero error, although geometric tolerances lead to very small errors that are first order with δ_z.
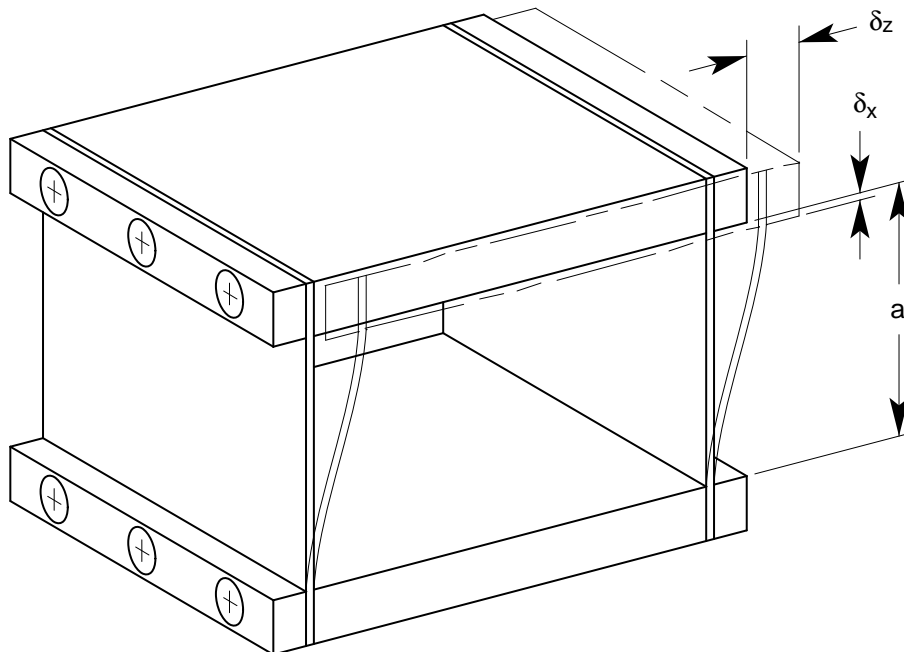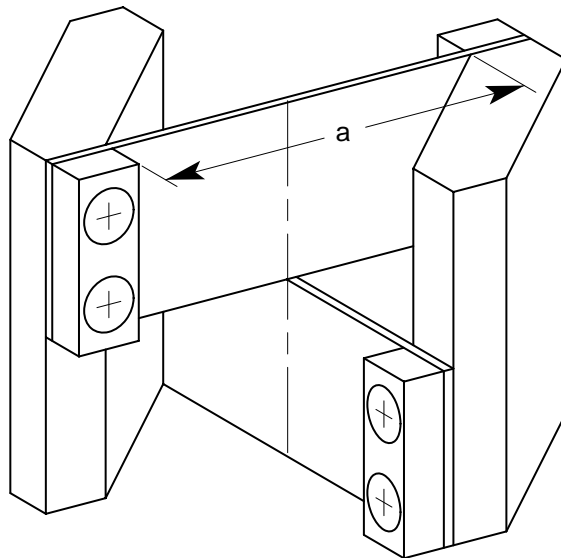

Figure 6-1 Two parallel blades allow one translational degree of freedom and constrain all others. This example shows bolted construction but monolithic designs are also common.

$$\delta_x = \int_0^a \left\{ 1 - \sqrt{1 - \left(\frac{dz}{dx}\right)^2} \right\} dx \cong \int_0^a \frac{1}{2}\left(\frac{dz}{dx}\right)^2 dx = \frac{3\delta_z{}^2}{5a} \tag{6.1}$$

Two cross blades, connected as shown in Figure 6-2, share one rotational degree of freedom. One blade constrains the degrees of freedom of the other that are not in common. Both blades redundantly constrain translation along the rotational axis. For a given rotation θ, each blade contributes a second-order radial displacement δ_r given by Equation 6.2. The first term inside the braces is the chord across a deflected blade while the second term is the comparable dimension produced by an ideal hinge. The net result is an extension rather than foreshortening as in parallel blades. The total error is the vector sum from both blades.

$$\delta_r = a\left\{ \frac{2}{\theta}\sin\left(\frac{\theta}{2}\right) - \cos\left(\frac{\theta}{2}\right) \right\} \cong \frac{a\,\theta^2}{12} \tag{6.2}$$

Figure 6-2 Two cross blades allow one rotational degree of freedom and constrain all others. This example shows bolted construction but brazed connections are common in commercial products.

Blades arranged axially, as shown in Figure 6-3, share one rotational degree of freedom. Two blades in different planes are sufficient to constrain the remaining degrees of freedom, but a symmetrical design with four blades is more common. This arrangement has nominally zero radial error motion in contrast to the cross-blade flexure. However, foreshortening of the blades in the axial direction presents an interesting compromise. Equation 6.3 shows the condition required to maintain equal foreshortening across the width of the blades. This condition is satisfied by joining the blades to parabolic-shaped flanges as Figure 6-3 (a) shows. Equation 6.4 shows the condition required to maintain equal bending stress across the width of the blades. The usual compromise solution is to join the blades to conical end caps as Figure 6-3 (b) shows. Making the blades relatively narrow improves this compromise but reduces the stiffness and load capacity of the flexure.

In addition, these equations suggest making the ratio a/r large, but they soon become invalid as the geometry diverges from normal beam theory. Finite element analysis is helpful in computing the bending stresses, but a linear code will not represent foreshortening in the blades and the axial stress that may result.

$$\delta_a(r) \cong \frac{3(r\,\theta)^2}{5a} \quad \to \quad a \propto r^2 \tag{6.3}$$

$$\sigma_b(r) \cong \frac{3\,E\,t(r\,\theta)}{a^2} \quad \to \quad a^2 \propto r \tag{6.4}$$

(a)   (b)
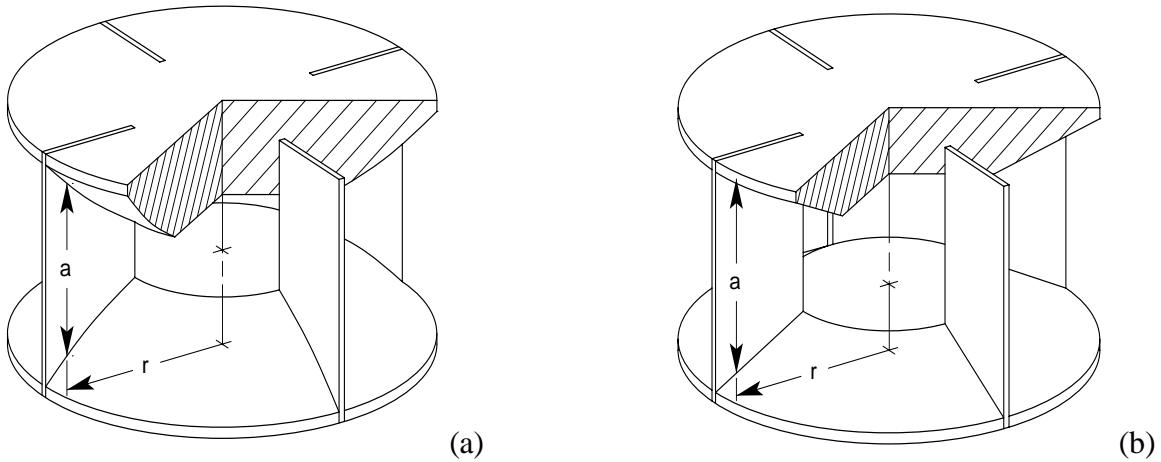
Figure 6-3 Axial blades allow one rotational degree of freedom and constrain all others. The shape of the flanges is important to the behavior of the flexure. In (a), two paraboloids that share a common vertex satisfy equal axial displacement across the blades. In (b), two cones that share a common vertex provide a reasonable compromise between equal axial displacement and equal bending stress across the blades.

6.1.2 Basic Kinematic Couplings

A kinematic coupling provides rigid and repeatable connection between two objects through usually six local contact areas. This is the case for the two traditional configurations shown in Figure 6-4: (a) the three-vee coupling and (b) the tetrahedron-vee-flat coupling (also known as the Kelvin clamp). The weight of the object being supported or some other consistent nesting force holds the surfaces in contact. A spring or compliant actuator may apply the nesting force, but ideally it should allow all surfaces to engage freely with minimum friction and wear. Otherwise, the coupling will not become *centered* as precisely as it should or perhaps not at all. Friction between the contacting surfaces acting on the compliance of the coupling is a main contributor to nonrepeatability as experimentally determined by [Slocum and Donmez, 1988].

The symmetry of three vees offers several advantages: better distribution of contact forces, better centering ability, thermal expansion about a central point and reduced manufacturing costs due to identical features. Conversely, the tetrahedral socket offers a

natural pivot point for angular adjustments. Many tip-tilt mirror mounts operate in this fashion. The three-vee coupling is the natural choice for adjustments in six degrees of freedom or when there is no need for adjustment.

(a)   (b)
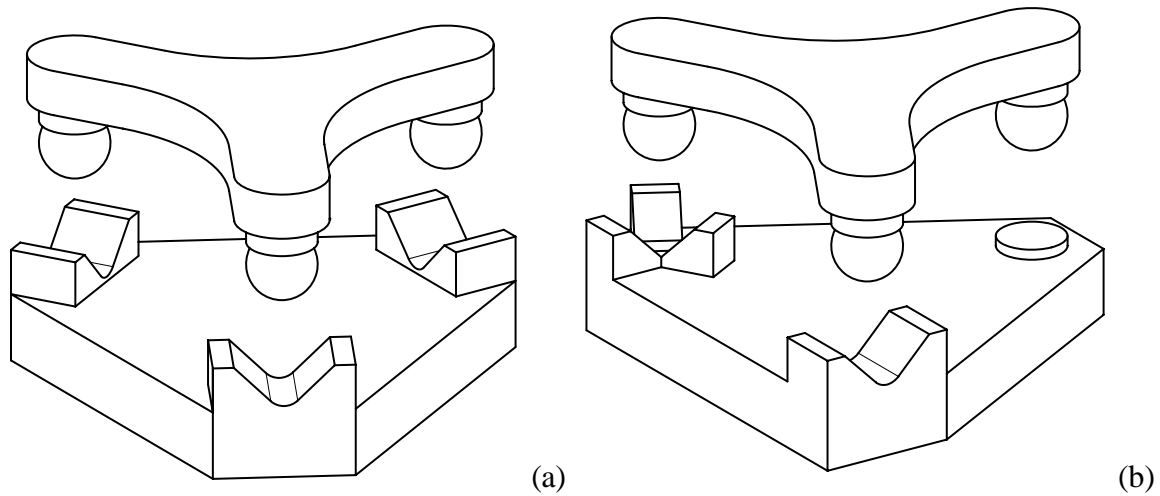
Figure 6-4 In (a), the three-vee coupling has six constraints arranged in three pairs. In (b), the tetrahedron-vee-flat coupling has six constraints arranged in a 3-2-1 configuration. Often for manufacturing reasons, the tetrahedron is replaced with a conical socket, hence the more familiar name cone-vee-flat.

The local contact areas of the traditional kinematic couplings are quite small and require a Hertzian analysis to ensure a robust design for the chosen material pair (see Appendix C, *Contact Analysis*). Greater durability is achieved by better curvature matching between contacting surfaces. Rather than use a full sphere against a flat surface, a partial sphere of much larger radius may be used instead. The same applies to cylindrical surfaces contacting with crossed axes. Another approach is to use a full sphere against a concave spherical or cylindrical surface. Figure 6-5 compares these two approaches for a vee constraint. Both constraints have the same relative (or effective) radius but the sphere in a gothic arch has less capture range.
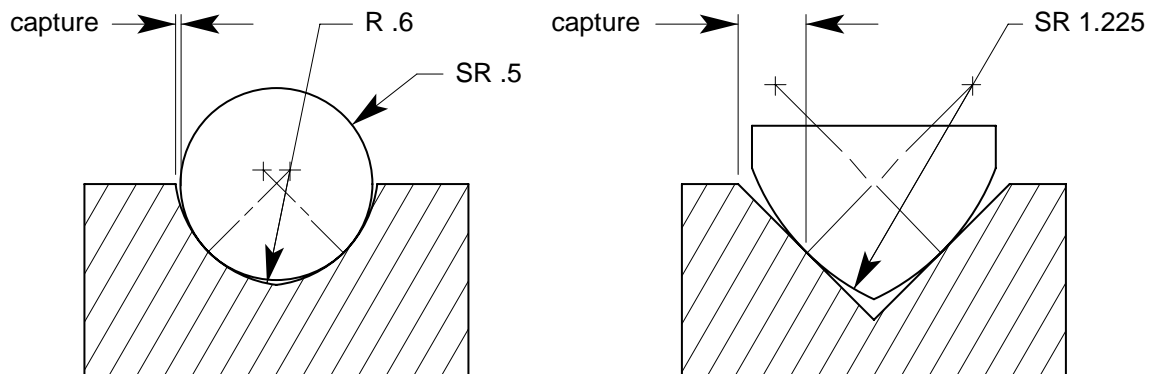
Figure 6-5 A vee constraint showing two ways to increase the area of contact. Capture is the maximum distance off center that the constraint will engage with tangency.

178

Designs based on line contact rather than point contact offer a significant increase in load capability and stiffness. For example, line contact forms between a precisely made, heavily loaded sphere and conical socket. The kinematic equivalent to three vees is a set of three sphere-cone constraints with either the spheres or the cones supported on radial-motion flexures. The upper member in Figure 6-6 (a) has six rigid-body plus three flexural degrees of freedom that three cones exactly constrain. Alternatively in (b), the three-tooth coupling forms three theoretical lines of contact between cylindrical teeth on one member and flat teeth on the other member. Each line constrains two degrees of freedom giving a total of six constraints. Manufactured with three identical cuts directly into each member, the teeth must be straight along the lines of contact but other tolerances may be relatively loose. Both of these kinematic couplings are being used on the EUVL project to overcome the limited hardness of super invar.

(a)   (b)
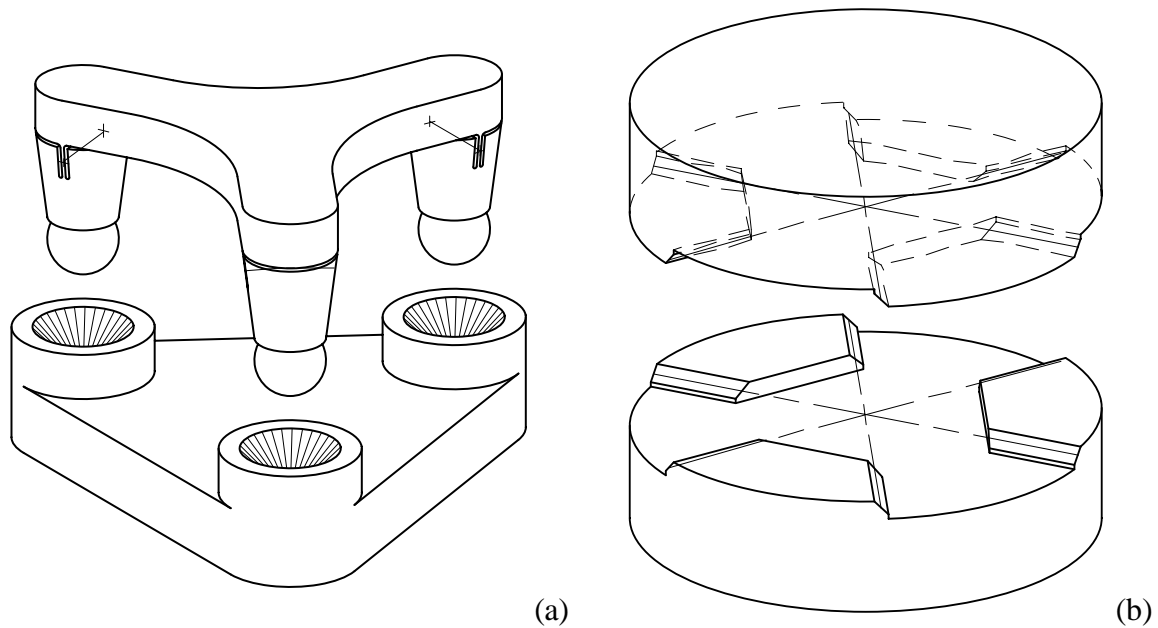
Figure 6-6 In (a), flexure cuts in the upper member allow each sphere limited radial freedom to seat in the conical sockets of the lower member. In (b), the three-tooth coupling forms three theoretical line contacts between cylindrical teeth on one member and flat teeth on the other member.

6.1.3 Extensions of Basic Types

Arranging constraints is a design process that requires a basic understanding of kinematics and the mechanics of constraint devices. The blade flexures and kinematic couplings presented thus far are good examples from which to learn and start new designs. This section presents several interesting and useful extensions based on three vee constraints. The examples range from fairly direct implementation on a touch trigger probe to a less obvious flexure stage with three degrees of freedom. In my experience, thinking of six constraints as three pairs has been a valuable and simplifying conceptual construct.

6.1.3.1 Touch Trigger Probe

Touch trigger probes are commonly used on coordinate measuring machines to indicate precisely where in the travel of the machine axes that contact is made with the workpiece. It is sufficient if the probe signal occurs with a known position lag as this is easy to correct in software. A common design studied by [Estler, et al., 1996, 1997] employs a three-vee kinematic coupling that acts as the electrical switch and the mechanical registration. The problem that Estler addresses through modeling and compensation is the variation in position lag depending upon the direction of travel, the orientation of the surface and other effects. A dominant error term, referred to as probe lobing, results from a three-fold variation in the trigger force acting on the compliance of the probe shaft.

The heart of the problem is the orientation of the vee constraints. Figure 6-7 shows the probe mechanism studied by Estler (a) and a new design (b) that solves probe lobing, at least in theory. In (a), the probe side of the coupling is preloaded down by a compression spring into three vee constraints represented by angled cylinders. The probe will not trigger until there is sufficient moment imparted to the coupling for any of the constraints to become unloaded, thus breaking electrical continuity. Although the preload is constant, the lever arm may vary up to a factor of two depending whether the coupling pivots about one vee or two. In (b), the new vee orientation requires a torsional preload to seat the coupling. In addition, the spring would be set to off-load the weight of the probe coupling. In this configuration, any applied moment (orthogonal to the preload) equally unloads one side of each vee; there is no directional preference. The downside will be a greater influence of friction since any pin must now slide up or down a vee rather than simply lifting out.
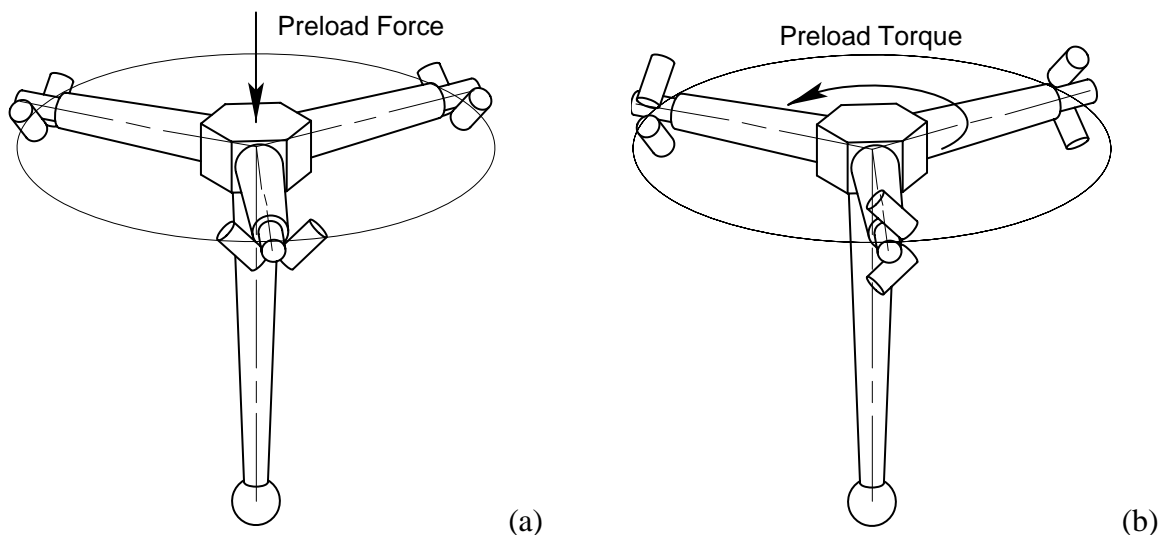
Figure 6-7 In (a), the moment required to unseat one vee while pivoting about the other two vees is a factor of two less than the moment required to unseat two vees while pivoting about the third vee. In (b), a moment applied about any axis in the plane of the vees produces equal reaction at all vees.

6.1.3.2 The NIF Diagnostic Inserter

The NIF requires a number of diagnostic instruments near the center of the 10 m diameter target chamber. Each instrument is transported approximately 6 m into the chamber by a telescoping diagnostic inserter. Since only the end position of travel requires submillimeter positioning, a kinematic coupling is being considered to provide repeatable registration at the end of a rather imprecise telescoping stage. However, the long, skinny geometry of the inserter presents an unfavorable aspect ratio for a traditional kinematic coupling. The configuration shown in Figure 6-8 was proposed to work within the geometric constraints yet provide acceptable moment stiffness and capacity. It was conceived by splitting the vees of a three-vee coupling and axially separating the odd-numbered constraints from the even-numbered constraints. The odd-numbered constraints act like a right-hand screw while the even-numbered constraints act like a left-hand screw. An applied axial preload force translates the cylinder until all constraints are engaged and an axial torque is established between the two sets of three constraints.
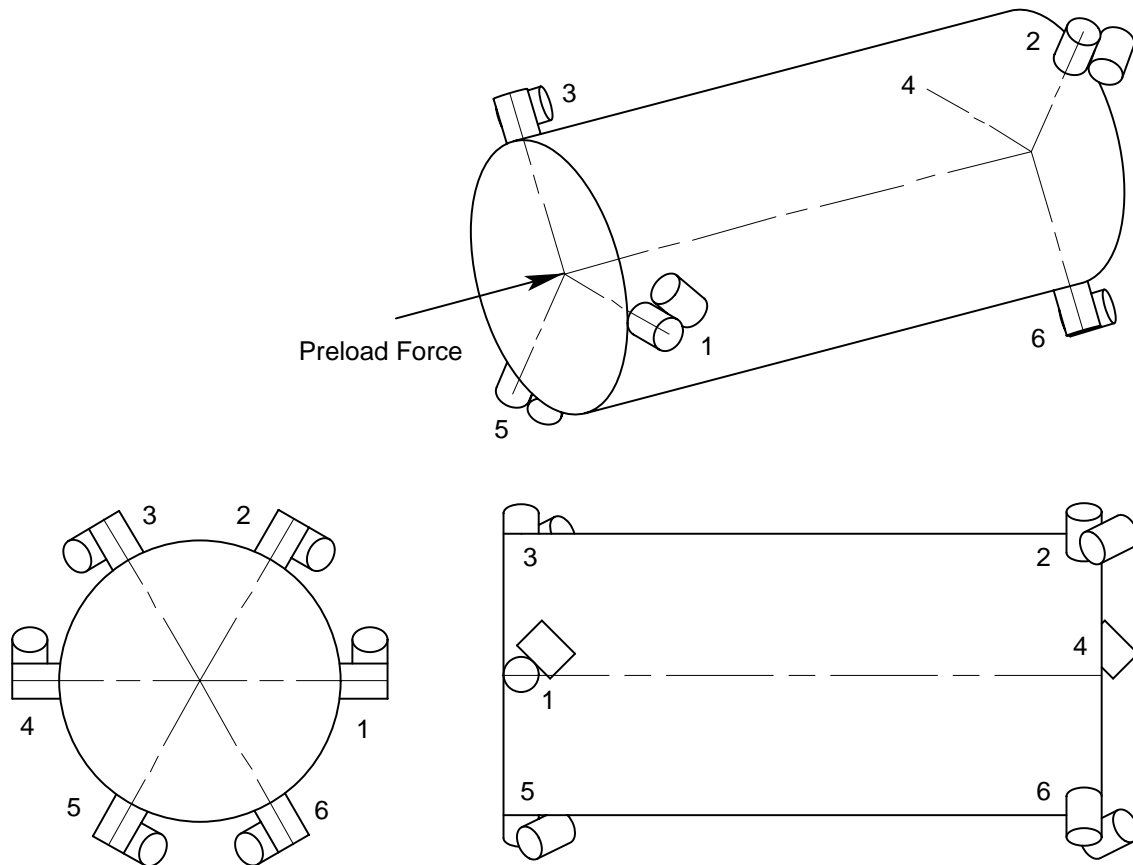
Figure 6-8 The end view looks much like a three-vee coupling with constraint pairs 2-3, 4-5 and 6-1 apparently forming three vees. The side view shows the significant separation between odd- and even-numbered constraints. As in Figure 6-7, the angled cylinders are constraints fixed to an unseen structure.

6.1.3.3 The NIF optics assembly

The NIF requires many hundreds of kinematic couplings to support large, replaceable optics assemblies. There are several types of kinematic couplings used throughout the system, but one in particular demonstrates a simple evolution from a basic three-vee coupling to a more novel configuration well suited for tall assemblies. Figure 6-9 shows the evolution in three simple steps. The horizontal configuration is convenient because gravity provides the preload. Rotating the coupling to the vertical configuration has obvious consequences, which motivates the next step to rotate the lower vees to carry the gravity load. It is important that the centroid of the supported object be offset from the lower vees in a direction that preloads the upper vee. The next step of spreading the upper vee has a particular advantage for NIF optics assemblies. The widely spaced vee provides frictional constraint that stiffens the torsional vibration mode of the optics assembly. This example appears again in Section 6.3.3 and Chapter 7.
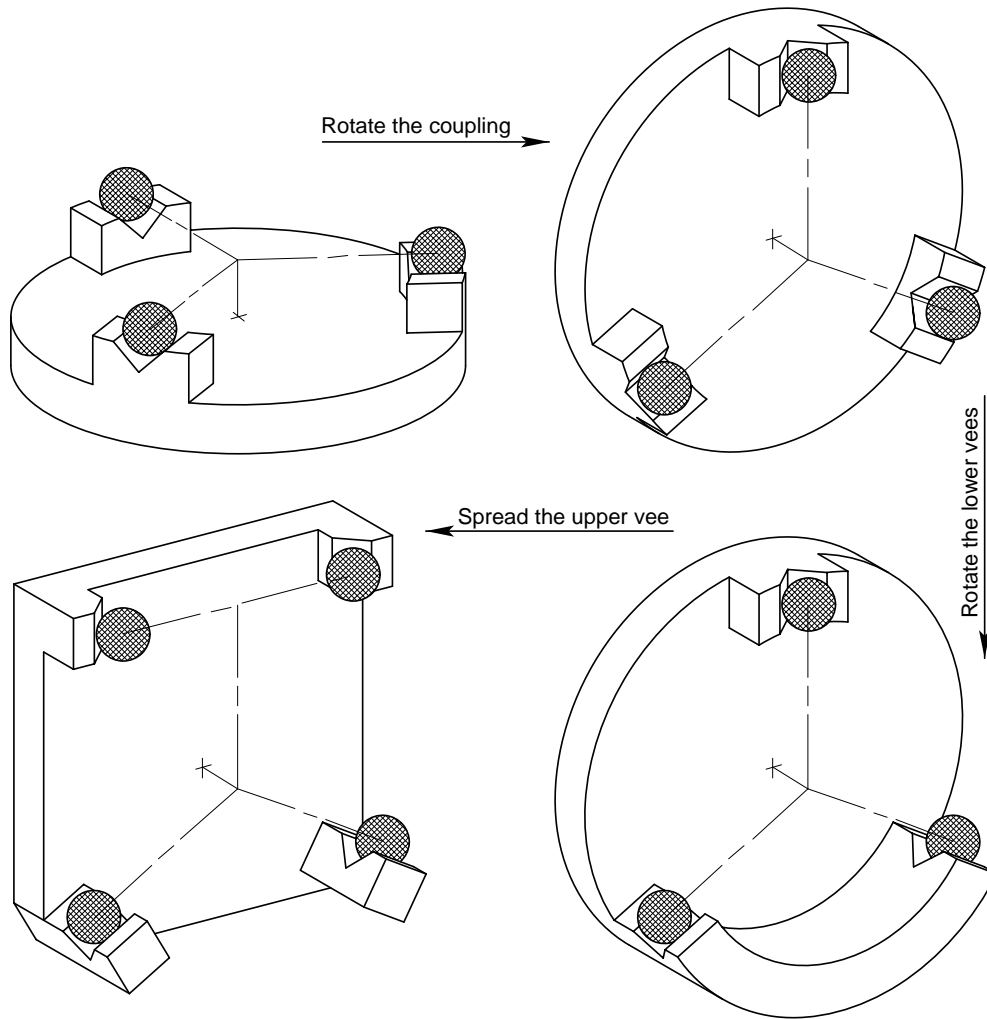
Figure 6-9 The evolution from a horizontal three-vee coupling to the configuration used for many NIF optics assemblies. The spheres in each configuration attach to the object being supported.

6.1.3.4 EUVL Mirror Mount

Friction between the contacting surfaces of a kinematic coupling is a disadvantage when it causes significant distortion in the precision component being supported. A common approach for mounting super-precision optics is an arrangement of three vee-flexures that [Vukobratovich and Richard, 1988] refer to as bipods. Figure 6-10 shows the bipod design used for EUVL mirror mounts. Each leg consists of four blades in series to provide one constraint and five degrees of freedom. One bipod provides the same constraint as a sphere and vee but without friction. Three bipods fully constrain the supported object with six constraints connected in parallel. Notice too that the top of the bipod has the features for a three-tooth coupling. There are mating features on the optic to provide the connect-disconnect function. The kinematic repeatability of the couplings ensure repeatable forces imposed by the bipod flexures on the optic, leading to a repeatable distortion between optic manufacturing and final use. This example appears again in Chapter 7 in greater detail.
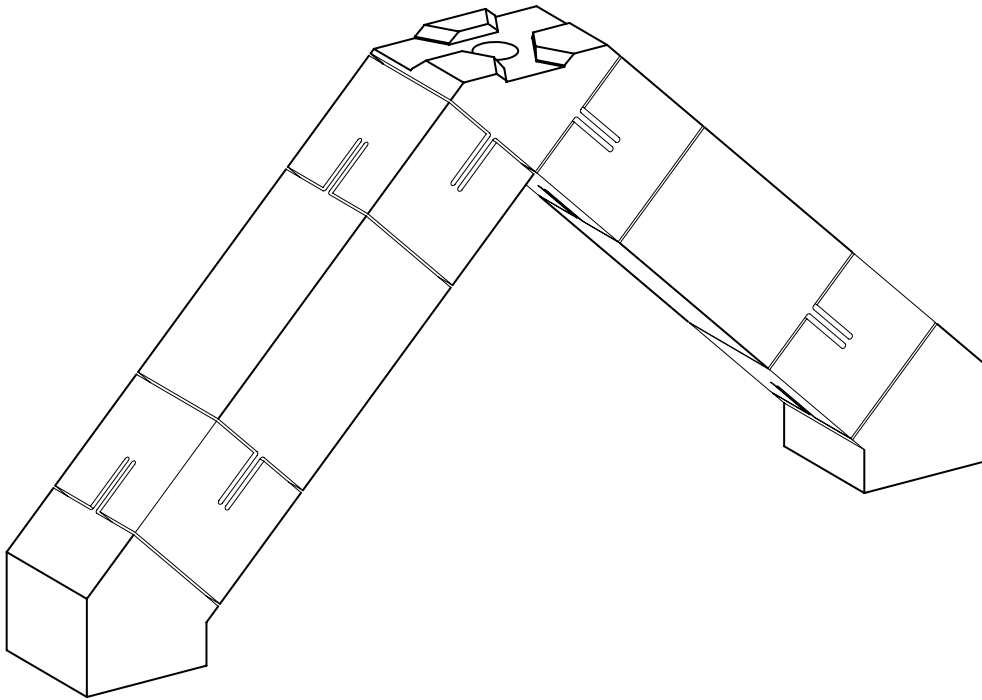

Figure 6-10 A single bipod flexure constrains two degrees of freedom in the plane of the vee. Usually the center section connects to the precision component and the ends connect to the support. At times it may be advantageous to reverse this role for better weight distribution provide by six supports.

6.1.3.5 X-Y-θ_z Flexure Stage

A flexure stage that provides pure planar motion (X-Y-θ_z) satisfies a number of applications found particularly in microelectronics and opto-mechanical systems. One approach to this problem is to serially connect single-axis flexure stages, for example, two sets of parallel blades and one set of cross blades. Besides being an awkward design, good stiffness in each constraint direction is difficult to obtain. When possible, it is better to arrange

constraints in parallel. An obvious example is a set of three single-constraint flexures arranged physically parallel to each other. This arrangement is rigid and simple, but has second-order, out-of-plane error motion that can only be reduced with longer constraints. A better arrangement appears in Figure 6-11. It consists of three folded-hinge flexures arranged as parallel constraints. This arrangement provides pure planar motion except for errors arising from geometric tolerances.
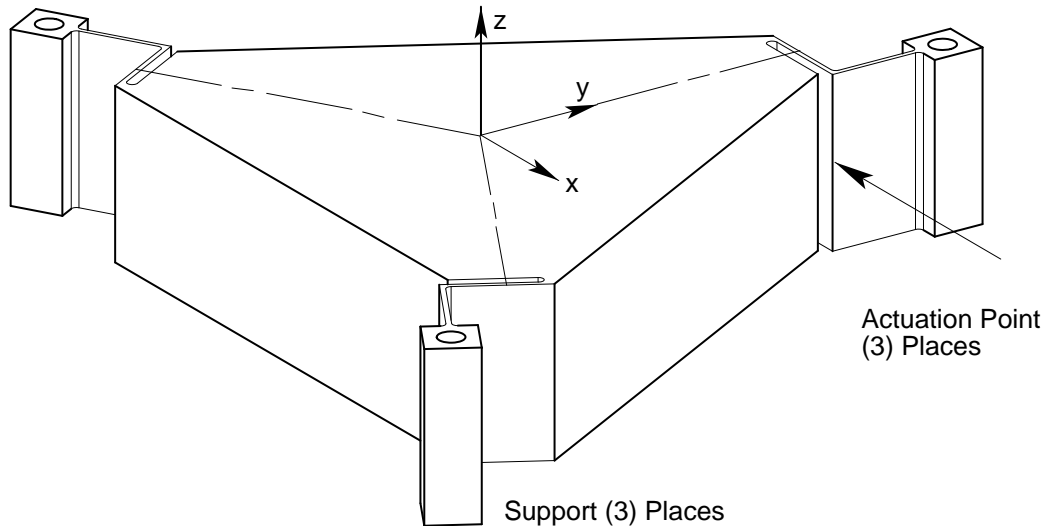
Figure 6-11 Three folded hinge flexures constrain motion within a plane and provide convenient points with which to actuate the stage.

The folded hinge provides one constraint although it appears compliant in all directions. Rather, the two blades have one degree of freedom in common so only five of the six (2 x 3 DOF) are independent. One nice feature of the folded hinge is the convenient point to apply actuation, for example, with a micropositioner. This was the approach used for an EUVL X-Y stage that appears in Chapter 7. [Ryu, Gweon and Moon, 1997] designed an X-Y-θ_z wafer stage that uses piezoelectric actuators driving folded hinges.

## 6.2 Analytical Design of Flexures

Much has been written about the analysis of flexures, so much so that the papers are seemingly saturated with the same information. There has been little new understanding presented in resent years. The emphasis in this section is in providing new information and understanding. This is accomplished using both beam theory and finite element analysis. A fundamental contribution is a matrix-algebra technique for modeling flexure systems. The equations for a blade flexure are contained in a compliance matrix and a stress matrix, both of which consider column effects. This is a sophistication not found in the formulas of Section 2.6. Computer software written for specific configurations such as the bipod flexure has proved very valuable in the case studies for this thesis. A general-configuration program for flexure systems, written in Mathcad™ Plus 6, appears in Section 6.3.

6.2.1 Comparison of Flexure Profiles

The blade flexures presented thus far have had constant thickness except perhaps near the ends where small fillets are typical. Another common flexure profile is the circular hinge, which typically is manufactured by drilling two adjacent holes to form the flexure and then by relieving other material as necessary to allow freedom of motion. The primary reference for the circular hinge is [Paros and Weisbord, 1965]. More recently, the elliptical hinge was studied by [Xu and King, 1996] and [Smith et al., 1997]. When the thickness of the flexure is small compared to the circle or ellipse, both of these profiles are well approximated by a parabola. A parabolic profile leads to simpler equations and better understanding. Since these three profiles have effectively the same performance, the circular hinge is the obvious choice for ease of manufacturing (whether by drilling holes or using circular interpolation). The interesting comparison is between the (circular, elliptical or parabolic) hinge flexure and the blade flexure because each has particular advantages.

To remain the most general, the presentation uses the elliptical profile described by the major and minor diameters a and b, respectively. For a circular profile, simply replace both a and b with the diameter d. Equation 6.5 gives the thickness profile for the ellipse and its approximate parabolic profile. Figure 6-12 compares these two profiles for an example that is near the limit for a good approximation. The approximation is better for a circular profile and of course when the minimum thickness t_0 is thinner. The straight lines in the figure have to do with the comparison to the equivalent blade flexure discussed later.

$$t_e = t_0 + b\left[1 - \sqrt{1 - \left(\frac{2x}{a}\right)^2}\right] \cong t_0 + \frac{b}{2}\left(\frac{2x}{a}\right)^2 = t_p \tag{6.5}$$
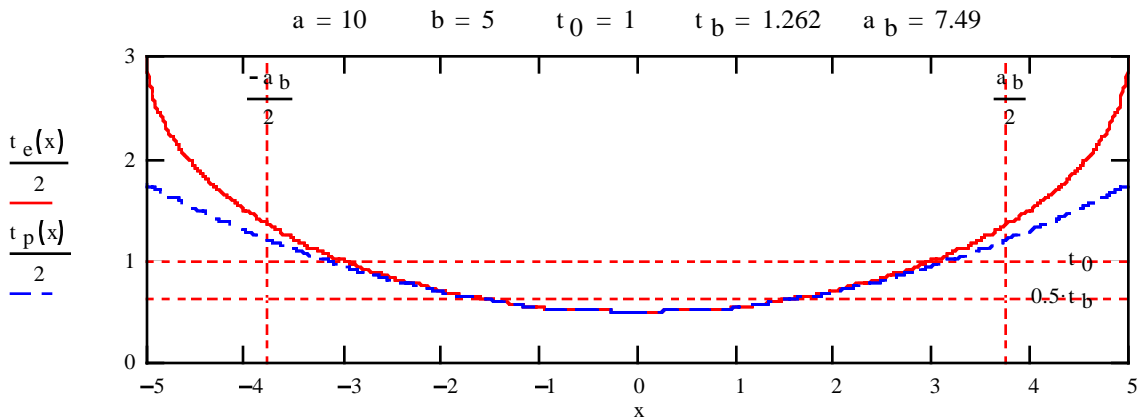
Figure 6-12 The solid line indicates the profile for one side of an elliptical hinge flexure. The horizontal axis is a plane of symmetry. The parabola (dash line) provides a good approximation in the thin region of the flexure that governs both the axial and moment compliance. The equivalent blade flexure is bounded by straight lines indicated by a_b and t_b.

Equations 6.6 and 6.7 give simplified expressions for axial compliance and moment compliance, respectively, for the parabolic profile. For this example, the axial compliance of

the ellipse is underestimated by 3% and the moment compliance is overestimated by 5% compared to *exact* solutions using the elliptical profile. However, the use of beam theory in the derivation is itself an approximation. These solutions are similar to those for the blade flexure. If the blade were taken to be of length a and thickness t_0, then the term in square brackets would represent the factor by which the hinge flexure was different.

$$c_x = \frac{1}{E\,w} \int_{-a/2}^{a/2} t_p^{-1} \, dx \cong \frac{a}{E\,w\,t_0} \left[\frac{\pi}{2} \sqrt{\frac{2\,t_0}{b}} - \frac{2\,t_0}{b} \right] \tag{6.6}$$

$$c_\theta = \left(1 - v^2\right) \frac{12}{E\,w} \int_{-a/2}^{a/2} t_p^{-3} \, dx \cong \left(1 - v^2\right) \frac{12\,a}{E\,w\,t_0^{3}} \left[\frac{3\,\pi}{16} \sqrt{\frac{2\,t_0}{b}} \right] \tag{6.7}$$

It is instructive to consider the length and thickness of a blade that is equivalent to the hinge flexure in terms of axial and bending compliance. The solution to two equations with two unknowns appears in Equation 6.8, where the subscript b indicates the equivalent blade parameters. This explains the straight lines in the figure marked with either a_b or t_b. The line marked t_0 indicates the part of the parabola that has the greatest slenderness ratio for buckling. The usual definition for slenderness ratio is the length divided by the minimum radius of gyration. Here it is more convenient to use the length divided by the thickness. It is obvious from the figure that the equivalent blade being both longer and thinner is more likely to buckle under a compressive load. Equation 6.9 gives the condition required for the hinge flexure to yield before buckling and the factor by which the equivalent blade flexure is more likely to buckle. For this example the factor is 1.88.

$$\frac{a_b}{a} \cong \sqrt{\frac{16}{3\,\pi} \frac{2\,t_0}{b} \left[\frac{\pi}{2} - \sqrt{\frac{2\,t_0}{b}} \right]^3} \qquad \frac{t_b}{t_0} \cong \sqrt{\frac{16}{3\,\pi} \left[\frac{\pi}{2} - \sqrt{\frac{2\,t_0}{b}} \right]} \tag{6.8}$$

$$SR_p \cong \frac{a}{\sqrt{2\,t_0\,b}} < \pi \sqrt{\frac{E}{12\,\sigma_y}} \qquad \frac{SR_b}{SR_p} \cong \pi - 2 \sqrt{\frac{2\,t_0}{b}} \tag{6.9}$$

The hinge flexure clearly has the advantage over the blade flexure for buckling resistance. The bending stress appears to be slightly higher for the thinner hinge flexure, since both equivalently require the same bending moment for a given rotation, but stress concentrations in the fillets of the blades can be just as high. The main advantage for the blade flexure comes when there is need for rotational flexibility about the axis of the blade, so as to twist. Of course the hinge flexure is better if the application calls for resisting twist. This is also true if the flexure is to be used as a secondary constraint in shear.

6.2.2 A Study on Fillets for Blade Flexures

Beam theory works well for blade flexures except at each end where there is a transition to some larger cross section. Monolithic blade flexures are usually manufactured with small corner radii know as fillets. Clamped blades, on the other hand, usually have very abrupt transitions that are difficult to model with any certainty. The edges of the clamping surfaces may have partial radii to transition the clamping force, but it is assumed that microslip will relieve the theoretically high stress concentration for axial and moment loads. Naturally the subject of this study is the behavior of fillets as a function of radius size. This is accomplished through a parameterized finite element model for one end of the blade.[I] In the study, the radius varies from one-half blade thickness to twice the blade thickness, and the model is subject to either axial or moment loading. Curve fits to the finite-element results are useful to supplement the limitations of beam theory.

An assumption is made in beam theory that either the out-of-plane stress or the out-of-plane strain is zero. The same is true for 2D FEA. The two choices bracket the range of a 3D model, plane stress for zero width and plane strain for infinite width. Both types were compared to a 3D model of varying widths. Consistent with the general practice in flexure design, plane stress is most appropriate in the calculation of axial stiffness and stress due to axial and moment loads. However, the results indicate that plane strain is more appropriate for moment stiffness, contrary to general practice. The effect is rather small, only 5 to 10 percent but in the nonconservative direction. Hence, the equations found in this thesis for bending of flexures have a factor $(1 - v^2)$ to account for stiffening due to the Poisson effect.[II] The same is true for the finite-element results that appear later in this section.

The shape of the transition region and the range of fillet radii are apparent in Figure 6-13. In this case, an axial load is applied to the left end of the 20 x 20 block, and the right end of the 2 x 10 blade is constrained. In Figure 6-14, opposite forces on the top and bottom of the block generate a moment load. Both figures show the deflected shape of the model and contours of von Mises stress. Although difficult to see, the maximum stress for axial loading occurs approximately at the quarter point of the fillet closest to the blade and occurs very near the start of the fillet for moment loading. The node on the lower right corner of the block is the displacement location used for the compliance calculations. All the results presented are normalized to the blade thickness *t* and calculations from beam theory.


[I] Pro/MECHANICA by Parametric Technology Corp. is the finite element software used in this study.

[II] The bending stress across the thickness of the flexure changes from tension to compression over a very short distance. The blade would bow if not connected on each end to a stiff structure. The plane-strain assumption does not allow any bowing so the calculation underestimates the desired quantity, bending compliance. The blade has some opportunity to bulge in width when axially loaded. The plane-stress assumption freely allows bulging so the calculation underestimates the desired quantity, axial stiffness. The maximum stress due to axial and moment loads occurs on the sides where the plane-stress assumption is valid.
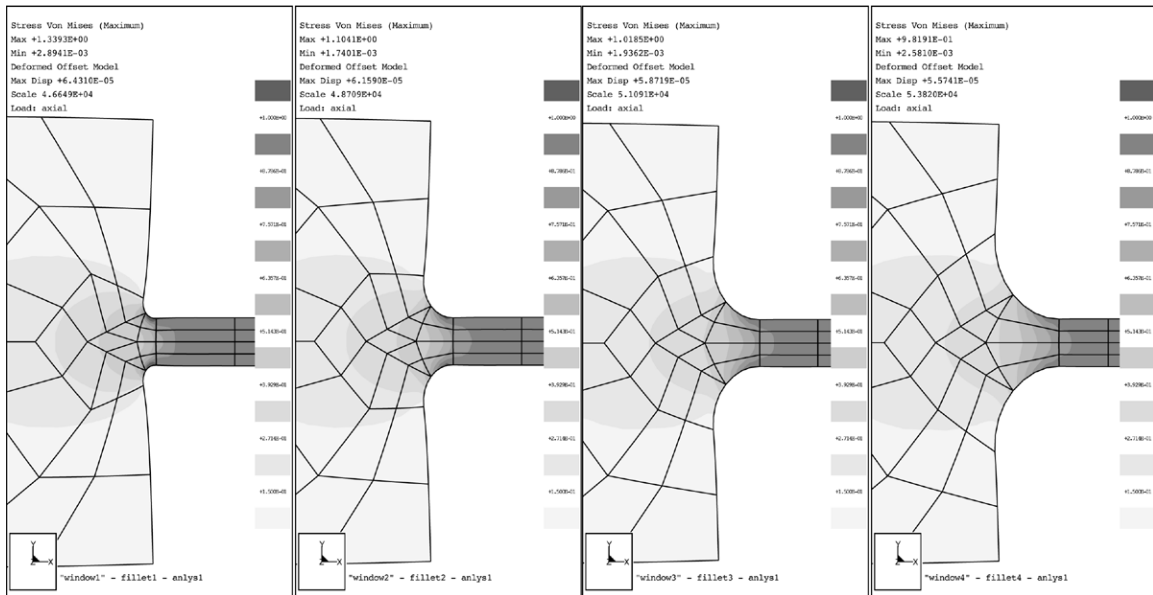
Figure 6-13 The fillet radii shown here are one-half, one, three-halves and two times the blade thickness. The deflected shape and the contours of von Mises stress result from an axial load.
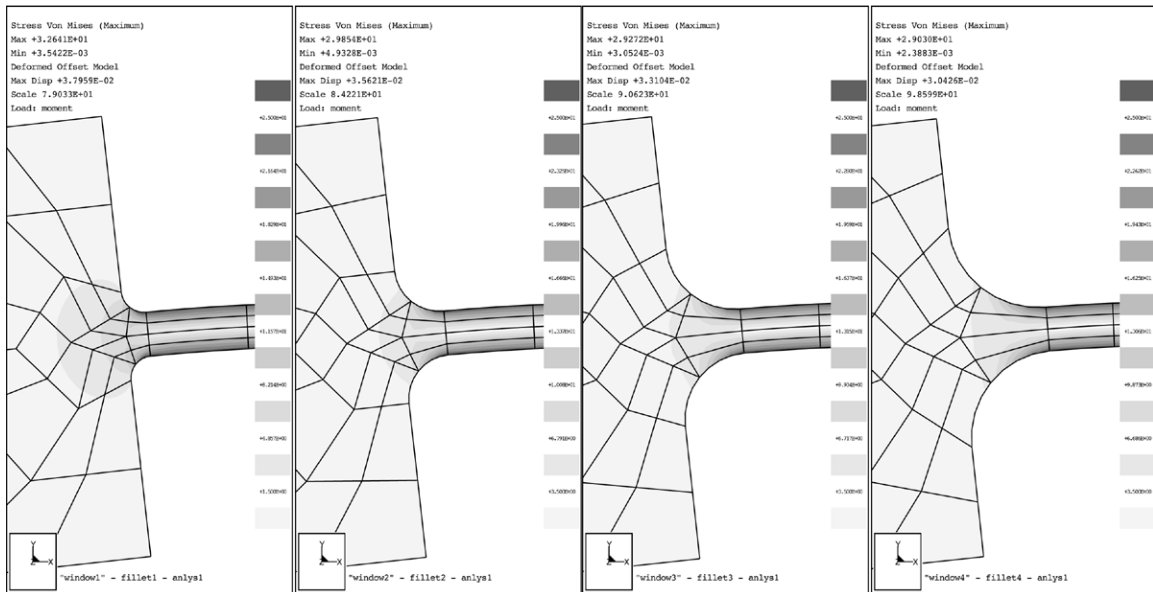

Figure 6-14 The fillet radii shown here are one-half, one, three-halves and two times the blade thickness. The deflected shape and the contours of von Mises stress result from a moment load.

The maximum stress from the 2D plane-stress model divided by the stress calculated from beam theory is the stress concentration factor plotted in Figure 6-15 for axial loading and Figure 6-16 for moment loading. In each graph, the solid line is a fitted curve to discrete results from the finite element model. The equation at the top of each graph may be used to calculate the stress concentration factor for any radius-to-thickness ratio between one-half and two. The knee in the curve appears to be at a ratio near one.
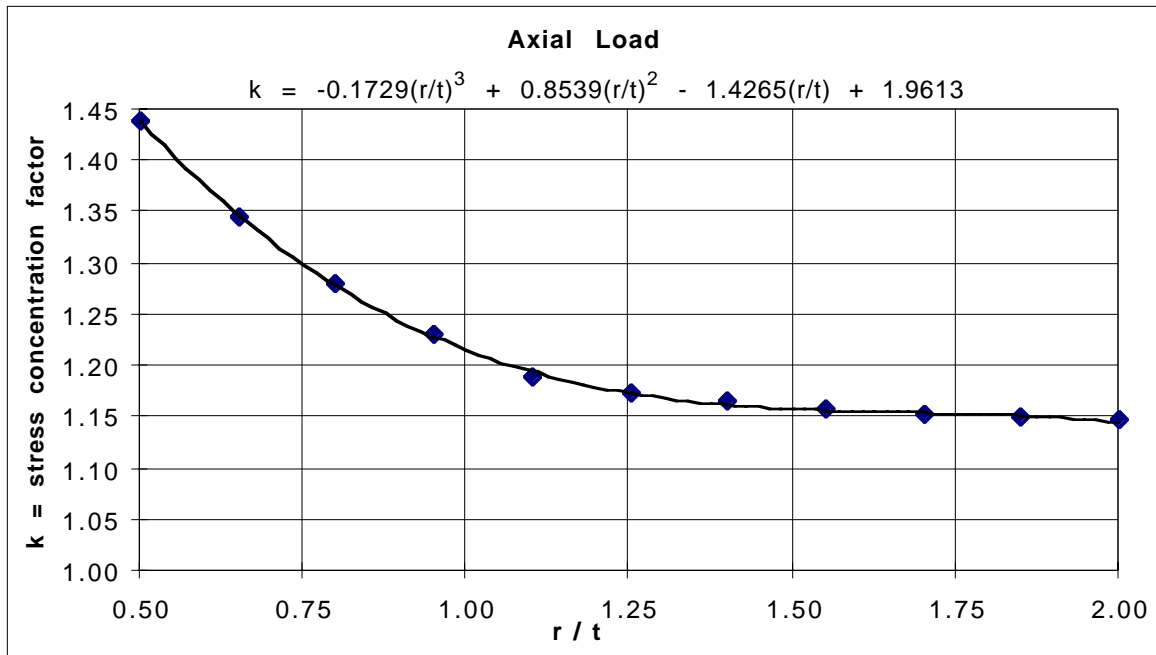
Figure 6-15 The stress concentration factor for axial loading is closely approximated by a cubic polynomial, where *r/t* is the ratio of fillet radius to blade thickness.
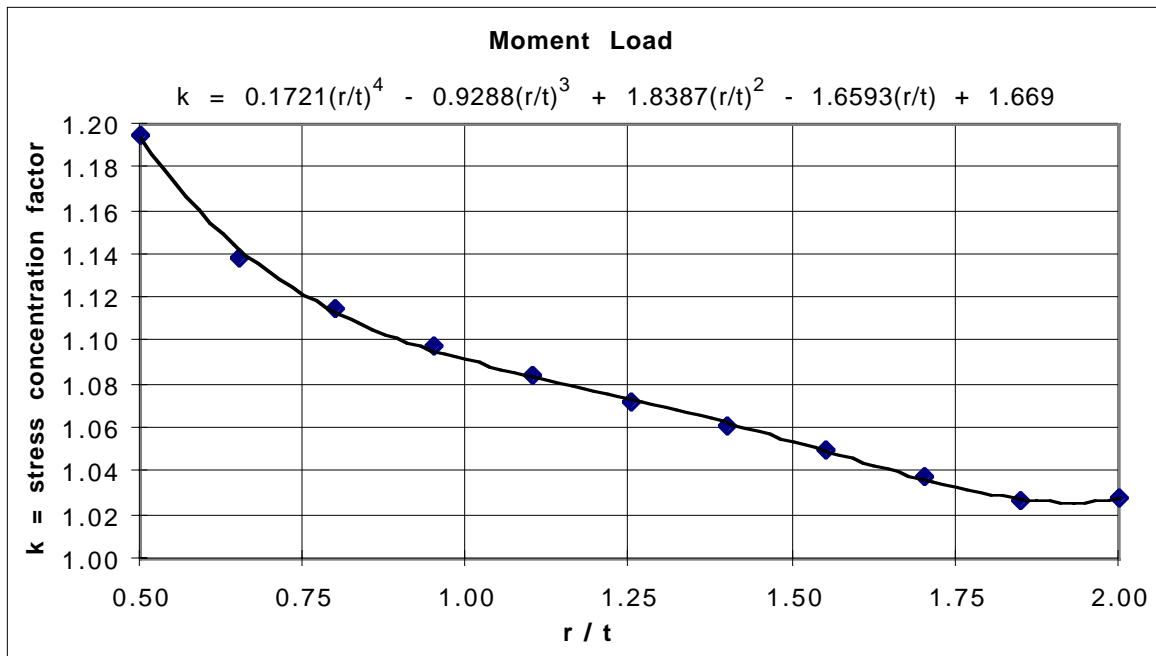
Figure 6-16 The stress concentration factor for moment loading is closely approximated by a fourth-order polynomial, where *r/t* is the ratio of fillet radius to blade thickness.

The size of the fillet radius also has an effect on the amount of deflection under load. A larger fillet shortens the effective length of the blade assuming that the end structures remain separated by a constant distance *a*. This effect on blade length is apparent in Figure 6-17 for axial loading and Figure 6-18 for moment loading. The curves give the

189

additional length of blade required to make beam theory match the displacement predicted from the finite element model. As might be expected, the compliance due to the elasticity of the end structures is significant for axial loading. For moment loading, beam theory matches the finite element model for a ratio $r/t = 0.62$.
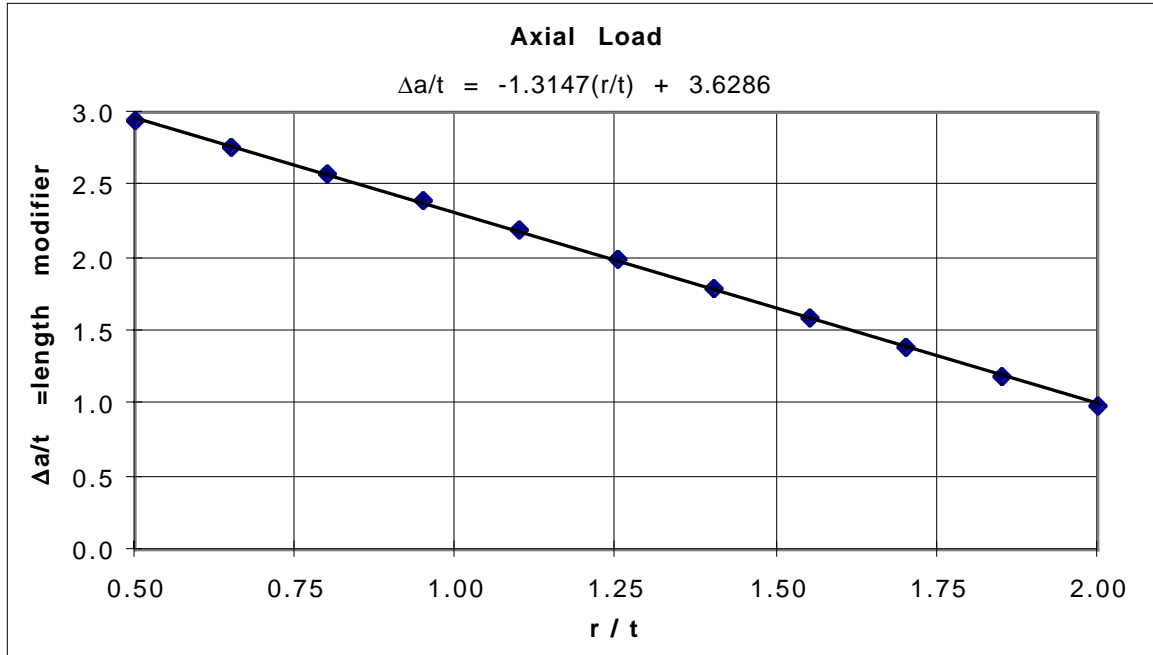
Figure 6-17 The length modifier for axial loading is closely approximated by a linear curve, where r/t is the ratio of fillet radius to blade thickness.

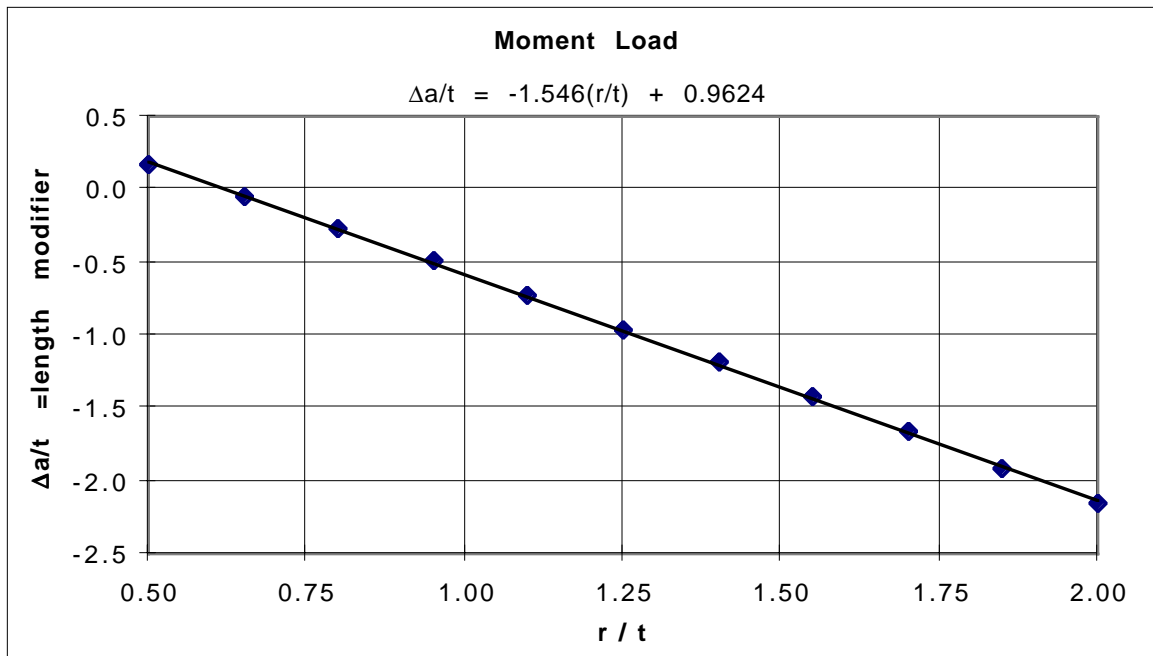**Figure 6-18** The length modifier for moment loading is closely approximated by a linear curve, where r/t is the ratio of fillet radius to blade thickness.

6.2.3 The Compact Pivot Flexure

An axial arrangement of two blades in series is a useful single-constraint device that provides angular freedom about three axes. Since the two translational degrees of freedom are rather stiff for short blades, it is common to duplicate another set of two blades some distance along the axial constraint direction. See, for example, the bipod flexure in Figure 6-16. The same cuts used to make the bipod flexure appear more clearly in Figure 6-19 (a). This basic design is being used on the NIF and EUVL projects. An advantage of this design becomes apparent when compared to the more common design in (b), where the axial compliance introduced at the junction between blades is significant. It clearly shows the compromise between axial stiffness and how closely spaced the blades can be. The design shown in (a), with much deeper end sections, greatly relieves this compromise. Even so, it starts to become an issue again when the blade is wider than four times its length. This three-dimensional behavior is best studied with 3D finite element analysis. As before, finite-element results are displayed so as to extend the usefulness of simple theory.

(a)   (b)
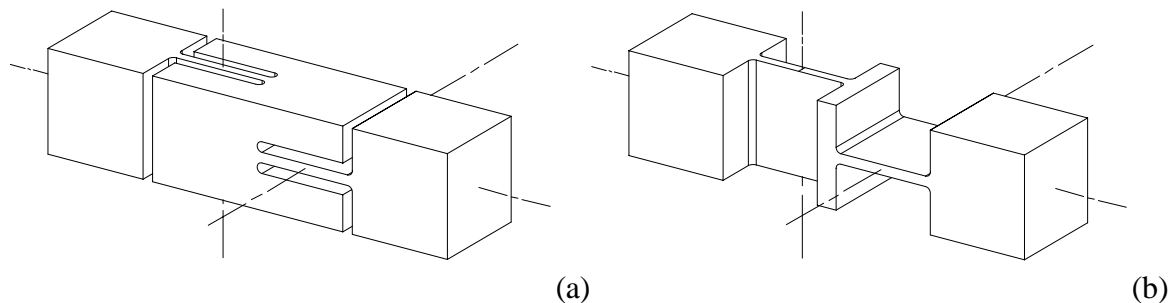
Figure 6-19 The design in (a) allows the minimum spacing of blades and maintains good axial stiffness. In addition, the gaps may be controlled to provide over-flexion protection. In order for the design in (b) to have good axial stiffness, the junction between blades would have to be lengthened.

Since only axial displacement is of interest in this study, the use of symmetry boundary conditions at two midplanes simplifies the model to just one-quarter the physical pivot flexure. This model, shown in Figure 6-20, also aids in viewing contours of von Mises stress through the blades. The variable parameter in this study is the blade width w, which varies from one to four times the length a. The blade length is ten times the thickness and the fillet radius is one-half the blade thickness.

Although the blades become stiffer with increasing width, the aspect ratio of the junction becomes less favorable and contributes a larger proportion to the total compliance. This is the reason in Figure 6-21 that the axial displacement when normalized to theory increases with blade width. This behavior is also apparent in von Mises stress as gradients that increase with blade width. Figure 6-22 shows how stress varies across the half-width taken through the center of the blade (length and thickness). Figure 6-23 shows how stress varies along the axis of symmetry. Notice that these stresses are away from the stress concentrations caused by fillets. A practical maximum for blade width is two times the length partly because the torsional stiffness increases rapidly with the ratio w/a.
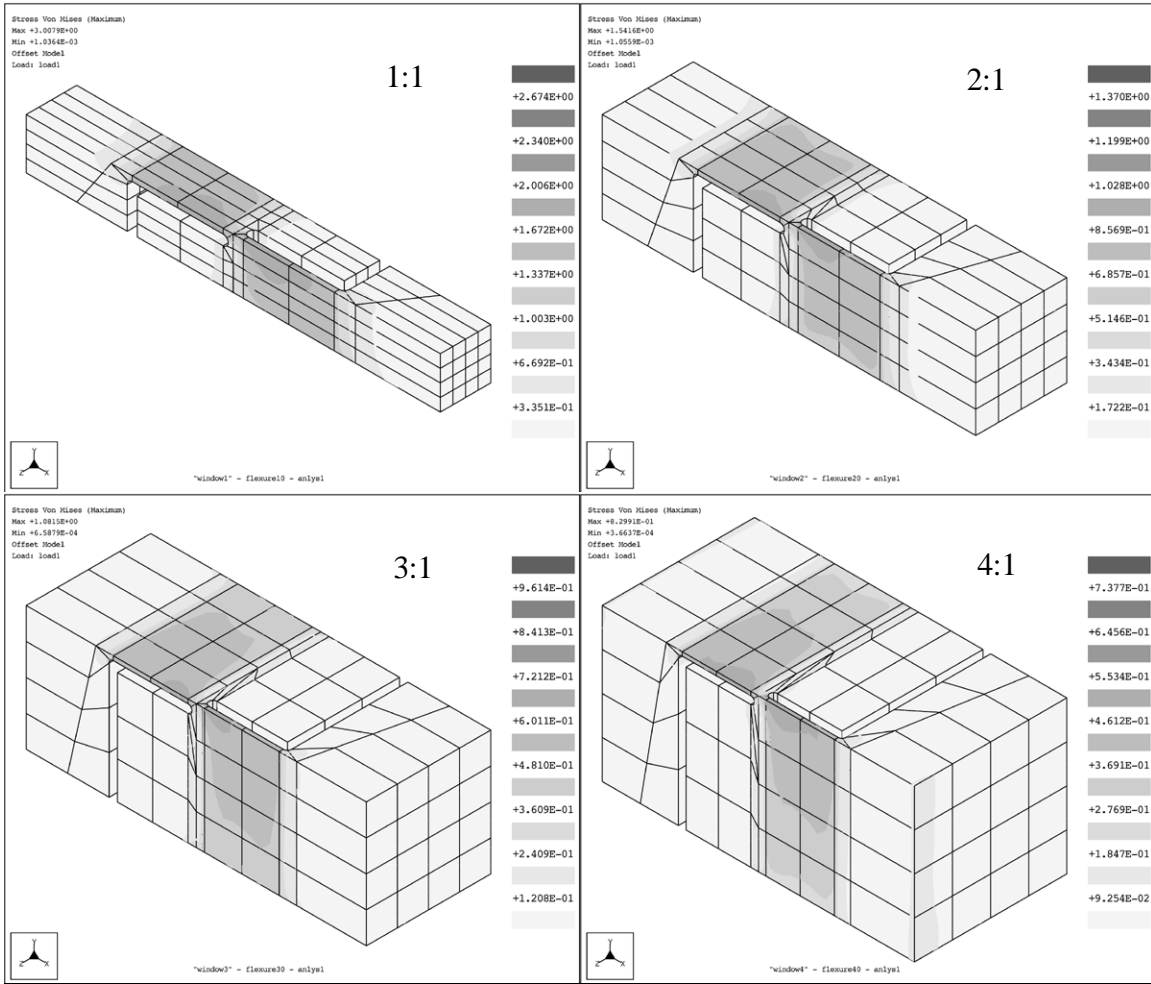
Figure 6-20 Contours of von Mises stress for blade widths from one to four times the blade length.
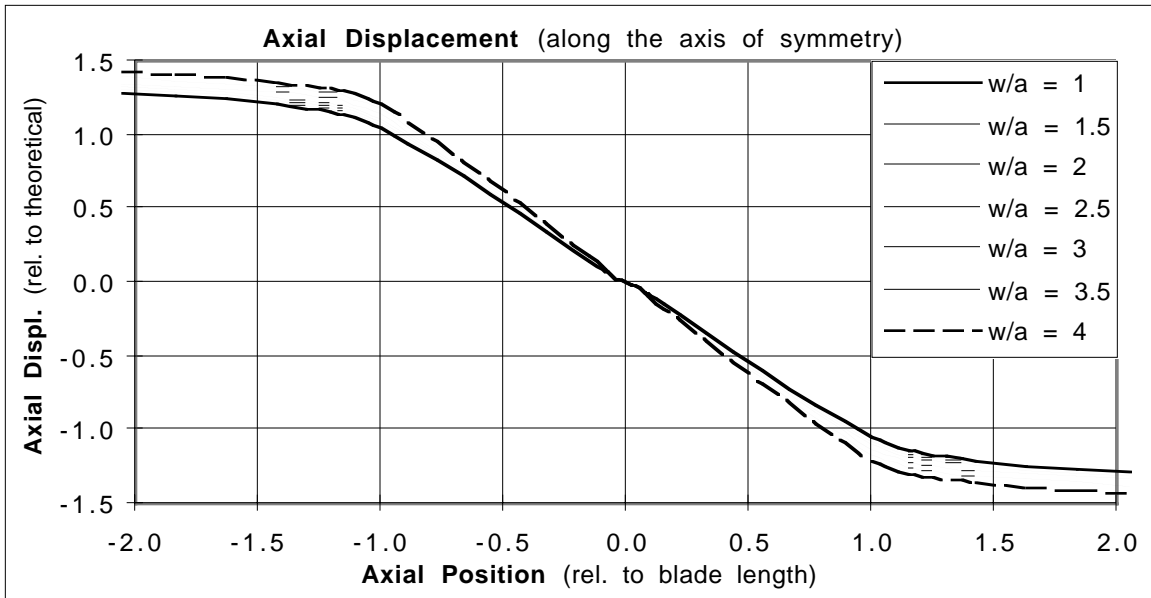

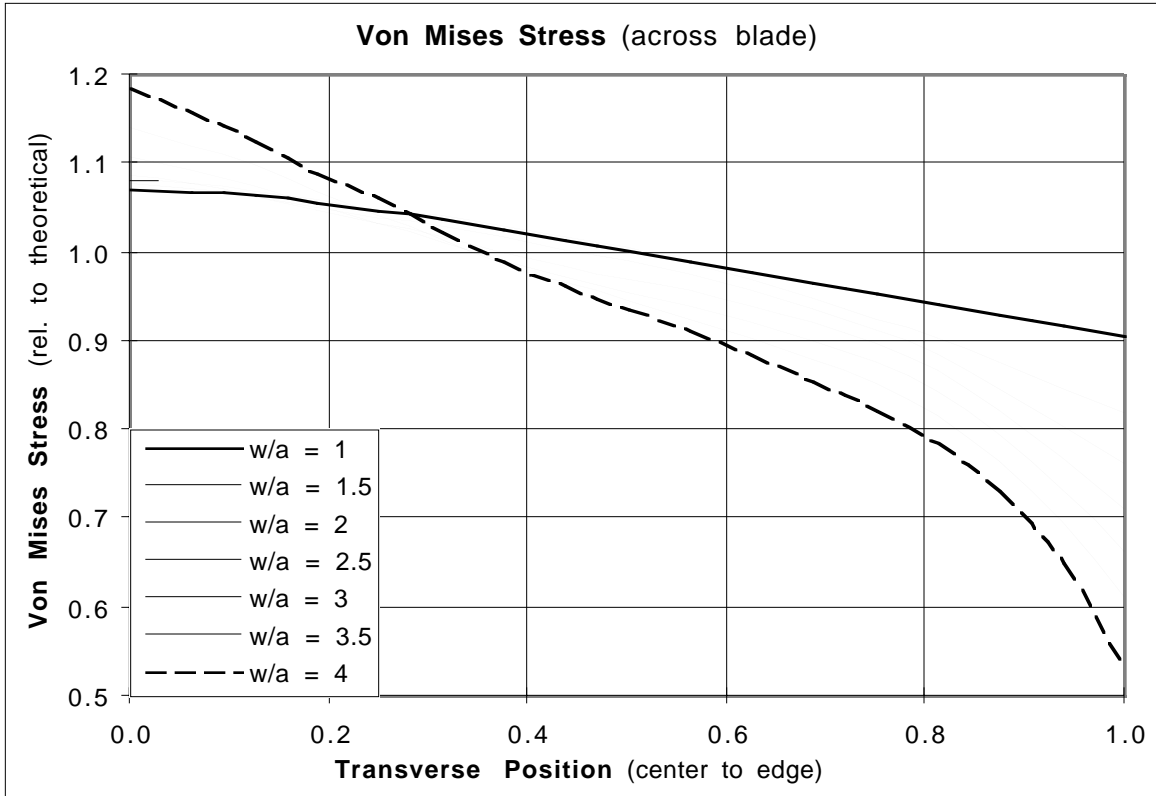**Figure 6-21** Axial displacement versus axial position along the axis of symmetry.

Figure 6-22 Von Mises stress versus position across the half width of the blade (taken at the mid length).
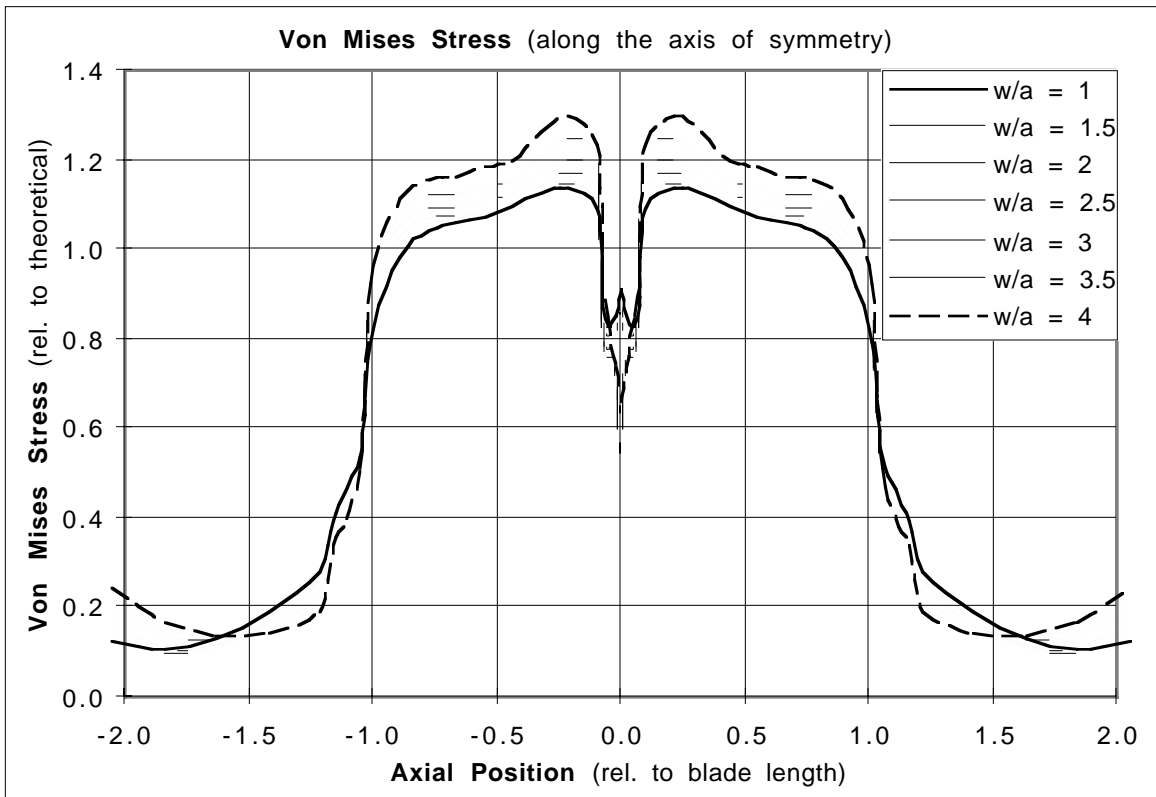

Figure 6-23 Von Mises stress versus position along the axis of symmetry.

6.2.4 Helical Blades for a Ball-Screw Isolation Flexure

The rather specialized application of a ball-screw (or leadscrew) isolation flexure motivated the development of an analytical model for a mildly helical blade flexure. Isolation flexures or bearing systems are commonly used on ultra-precision machines to couple only the desirable degrees of freedom between a ball screw and the carriage it drives [Slocum, 1992]. For different reasons, a recent paper demonstrated a clever way to improve the resolution of a leadscrew by effectively placing a flexural leadscrew in series with the mechanical leadscrew [Fukada, 1996], although no words to this effect are mentioned. While the screw-nut interface requires some level of torque before sliding takes place, the flexural leadscrew responds to arbitrarily small torque to give arbitrarily small resolution. Both of these valuable functions, exact constraint and smaller resolution, can be achieved in one simple device using a set of helical blade flexures. This idea is being used on the NIF precision linear actuator (see Chapter 8.5).
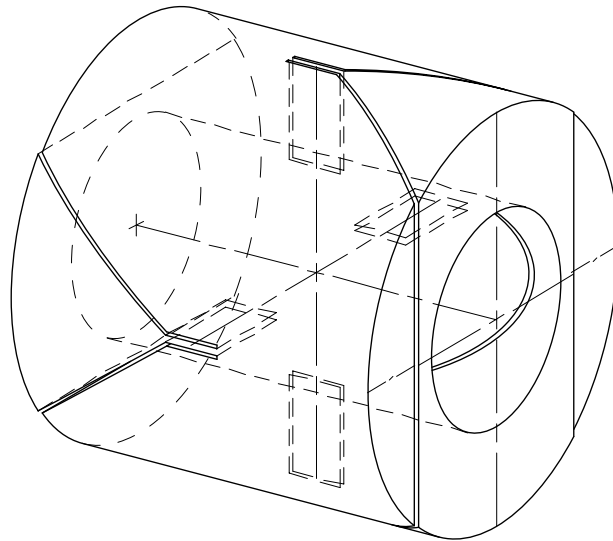
Figure 6-24 The ball-screw flexure for the NIF precision actuator requires two rotational degrees of freedom, a primary constraint against translation along the screw, and secondary constraints for the remaining degrees of freedom. Note, some hidden lines were removed to better show the main features.

Figure 6-24 shows the basic flexure design used for the NIF actuator. It resembles the compact pivot flexure of the last section except that it is hollow to allow the ball screw to pass through. In addition, the two hinge axes intersect to maximally condense the overall length, but this is not required in general. On the NIF actuator, there is another pivot some distance beyond the end of the screw so that the pivot pair provides free translation. Ordinarily the ball-screw flexure would have two pivots to provide free translation. Although it is not apparent from the figure, the blades are manufactured with a slight helix angle. Conceptually, if the blades were concentrated at the pitch diameter of the screw, then the proper helix angle would be perpendicular to the helix of the screw. Since the blades must lie outside the screw, then the actual helix angle must be somewhat smaller. This

condition does two things simultaneously: it aligns the blades to the reaction force; and it aligns out-of-plane motion of the blades to an insensitive direction of the screw. Effectively this creates a flexural screw with the same lead as the mechanical screw. Either one or both can be active since they appear the same to the system.

Before getting into the nature of helical blades, it is instructive to look over the finite-element results in Figure 6-25 for the one-quarter model. The von Mises stress plot in (a) highlights the blades but the point to notice is the gradient across the width. This is an indication of the relative flexibility of the annular junction between the two blades. The axial displacement plot in (b) shows a gradient along the length of each blade and nearly as significant a change in shading through the annular junction. Again this points to the annular junction as being a challenge to make much stiffer than the blades. There is some advantage to using a square cross section rather than an annulus if space permits.
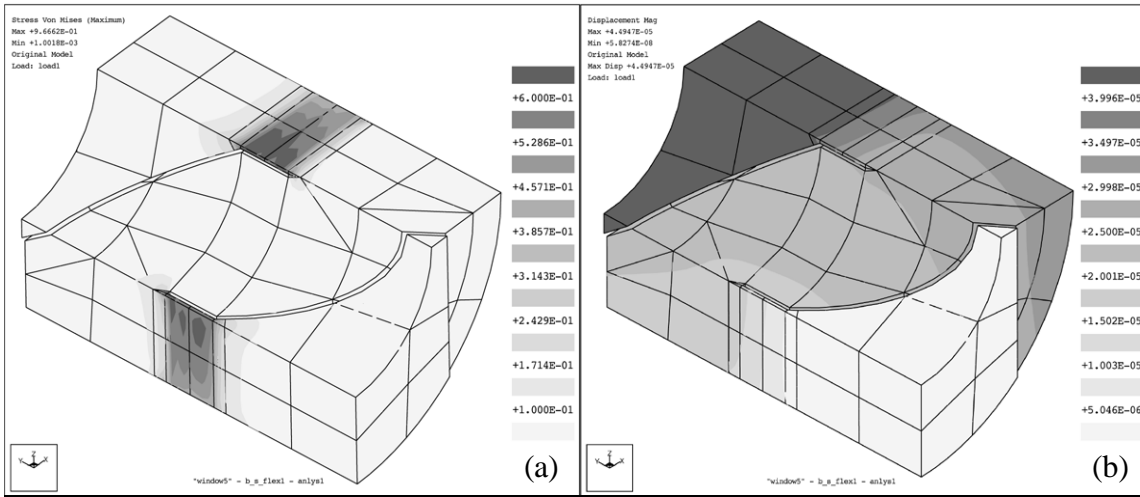
Figure 6-25 Contours of von Mises stress (a) and axial displacement (b) show the basic behavior.

Usually a blade flexure is initially straight so that a small out-of-plane displacement gives only a second-order axial displacement. The helical blade flexure is deliberately inclined with respect to the axis so that a small component of the out-of-plane displacement is along the axis. The angle of inclination varies with radius approximately as r θ/a using the parameters in Figure 6-26. The out-of-plane displacement also varies with radius in a way that compounds with the inclination. Using similar triangles, it is simple to relate the differential motion at any radius to the parameters of the flexure. This relation is then applied to the one particular radius $\bar{r}$ that has no net strain along the blade. The result is the effective lead of the flexure given by Equation 6.10.

$$L \equiv 2\pi\frac{\mathrm{d}x}{\mathrm{d}\theta} = 2\pi\,\bar{r}^2\frac{\theta}{a} \tag{6.10}$$
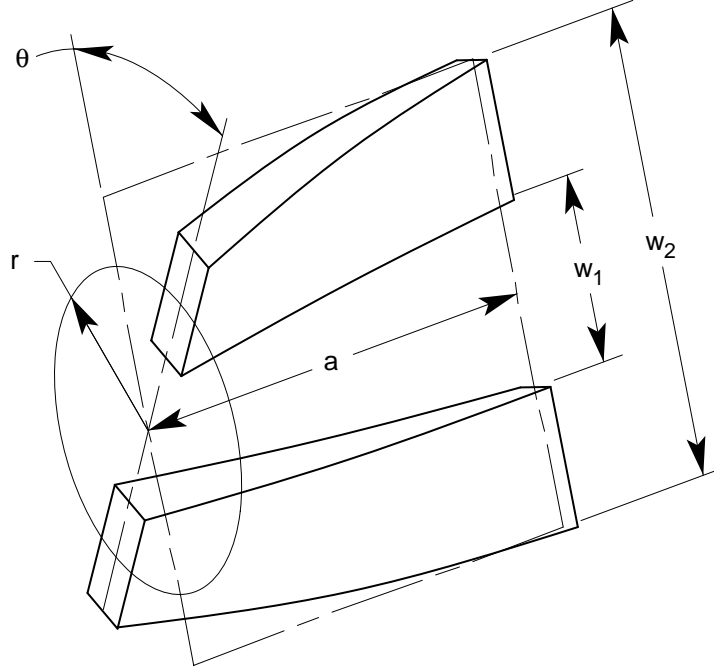
Figure 6-26 The effective lead of a helical blade flexure is governed by the parameters a, w_1, w_2, and θ.

To go further requires an assumption that the ends are constrained to remain parallel. Again using similar triangles, it is simple to determine the axial strain at any radius. Since the flexure is in equilibrium, the axial strain integrated over the cross section must be zero as indicated in Equation 6.11. Upon solving, Equation 6.12 gives the radius for zero strain, which then may be substituted back into Equation 6.10.

$$0 = \int_{r_1}^{r_2} \frac{\partial \varepsilon}{\partial \theta}\, dr = \int_{r_1}^{r_2} \left\{ \frac{\left(r^2 - \bar{r}^2\right)\theta}{a^2 + (r\theta)^2} \right\} dr \cong \frac{\theta}{a^2 + (\bar{r}\theta)^2} \int_{r_1}^{r_2} \left(r^2 - \bar{r}^2\right) dr \tag{6.11}$$

$$\bar{r}^2 \cong \frac{1}{3}\left(r_1^2 + r_1 r_2 + r_2^2\right) = \frac{1}{6}\left(w_1^2 + w_1 w_2 + w_2^2\right) \tag{6.12}$$

The axial strain that results from the helical shape also acts to stiffen the flexure in torsion beyond that for a flat blade. The approach used in Equation 6.13 to compute this effect is essentially a strain energy method (Castigliano's first theorem). The additional torsional stiffness due solely to the helix correctly goes to zero as the lead of the screw goes to zero.

$$k_{\theta_{helix}} = 2E\,t\,a \int_{r_1}^{r_2} \left(\frac{\partial \varepsilon}{\partial \theta}\right)^2 dr \cong 2E\,t\,a \left\{ \frac{\theta}{a^2 + (\bar{r}\theta)^2} \right\}^2 \int_{r_1}^{r_2} \left(r^2 - \bar{r}^2\right)^2 dr$$

$$\cong \frac{E\,t\left(w_2 - w_1\right)^3}{12\,a}\left(\frac{4w_1^2 + 7w_1 w_2 + 4w_2^2}{5w_1^2 + 5w_1 w_2 + 5w_2^2}\right)\left\{ \frac{2\pi\bar{r}}{L} + \frac{L}{2\pi\bar{r}} \right\}^{-2} \tag{6.13}$$

6.2.5 A General Approach for Analyzing Flexure Systems

The most general approach for analyzing a flexure system is finite element analysis. Arbitrarily large, complex systems to very simple systems are readily modeled with commercial FEA software. For example, blade flexures typically modeled with shell elements are connected as necessary to other shell and/or solid elements to represent the whole system. It is hard to imagine a more flexible way to accurately analyze deflections and stresses in some spatially complex arrangement of flexures. Yet in several respects the approach presented here is more flexible than FEA especially early in the design cycle. The model is completely parametric and represents only the elements of interest, usually the flexures. It reports the stiffness and compliance matrices for the constrained system, and it includes column effects that a linear FEA code cannot. The main drawback is that the user must understand the basics of matrix algebra and transformation matrices, which is transparent to the user of an FEA code.

The basic assumption is that the flexure system can be modeled as parallel and series combinations of springs and that an equivalent spring for the system represents useful information, for example, the stiffness matrix. If desired, that information can be propagated back to individual springs, for example, to obtain local forces and moments. The key formalism in this approach is the six-dimensional vector used to succinctly represent three linear degrees of freedom and three angular degrees of freedom. We will deal strictly with force-moment vectors and differential displacement-rotation vectors. These vectors are related through the stiffness matrix or the compliance matrix of the spring. The concept of a three-dimensional stiffness matrix as expressed in Equation 6.14 may be more familiar. The six-dimensional stiffness matrix is assembled as blocks of three-dimensional matrices as Equation 6.15 shows. At times it may be easier to start by building the compliance matrix as in Equation 6.16. Converting from one to the other requires inverting the whole matrix rather than inverting separate blocks.

$$\mathbf{f} = \begin{bmatrix} f_x \\ f_y \\ f_z \end{bmatrix} = \begin{bmatrix} k_{xx} & k_{xy} & k_{xz} \\ k_{xy} & k_{yy} & k_{yz} \\ k_{xz} & k_{yz} & k_{zz} \end{bmatrix} \cdot \begin{bmatrix} \mathrm{d}\delta_x \\ \mathrm{d}\delta_y \\ \mathrm{d}\delta_z \end{bmatrix} = \mathbf{K_{f/\delta}} \cdot \mathrm{d}\delta \qquad (6.14)$$

$$\begin{bmatrix} \mathbf{f} \\ \hline \mathbf{m} \end{bmatrix} = \begin{bmatrix} \mathbf{K_{f/\delta}} & \vdots & \mathbf{K_{f/\theta}} \\ \hline \mathbf{K_{m/\delta}} & \vdots & \mathbf{K_{m/\theta}} \end{bmatrix} \cdot \begin{bmatrix} \mathrm{d}\delta \\ \hline \mathrm{d}\theta \end{bmatrix} \qquad \mathbf{K_{m/\delta}} = \mathbf{K_{f/\theta}}^{\mathrm{T}} \qquad (6.15)$$

$$\begin{bmatrix} \mathrm{d}\delta \\ \hline \mathrm{d}\theta \end{bmatrix} = \begin{bmatrix} \mathbf{C_{\delta/f}} & \vdots & \mathbf{C_{\delta/m}} \\ \hline \mathbf{C_{\theta/f}} & \vdots & \mathbf{C_{\theta/m}} \end{bmatrix} \cdot \begin{bmatrix} \mathbf{f} \\ \hline \mathbf{m} \end{bmatrix} \qquad \mathbf{C_{\theta/f}} = \mathbf{C_{\delta/m}}^{\mathrm{T}} \qquad (6.16)$$

Once the stiffness matrix or the compliance matrix is formed in one coordinate system (CS), it is a simple matter using the [6 x 6] transformation matrix to reflect it to any another (CS). Once expressed in the same CS, stiffness matrices are added to represent

parallel combinations, and compliance matrices are added to represent series combinations. This process is expressed in Equations 6.17 and 6.18 (also A.35 and A.36). Mixed combinations of parallel and series springs require like groups to be combined first then inverted as necessary to complete the combination. See Appendix A for a complete discussion of transformation matrices and parallel and series combinations.

$$\mathbf{K}_0 = \sum_i \mathbf{T}_{0/i} \cdot \mathbf{K}_i \cdot \mathbf{T}_{0/i}^{\mathrm{T}} \tag{6.17}$$

$$\mathbf{C}_0 = \sum_i \mathbf{T}_{0/i}^{-\mathrm{T}} \cdot \mathbf{C}_i \cdot \mathbf{T}_{0/i}^{-1} \tag{6.18}$$

The remainder of this section focuses on the details that make this approach truly useful. The first task is to derive the compliance matrix for the blade flexure. The solution depends on the CS so naturally we will choose the simplest one. Similarly, the stress matrix is derived so that maximum stresses in the blade are easy to calculate. Finally the details of constructing parallel-series spring models are presented.

6.2.5.1 The Compliance Matrix for a Blade Flexure
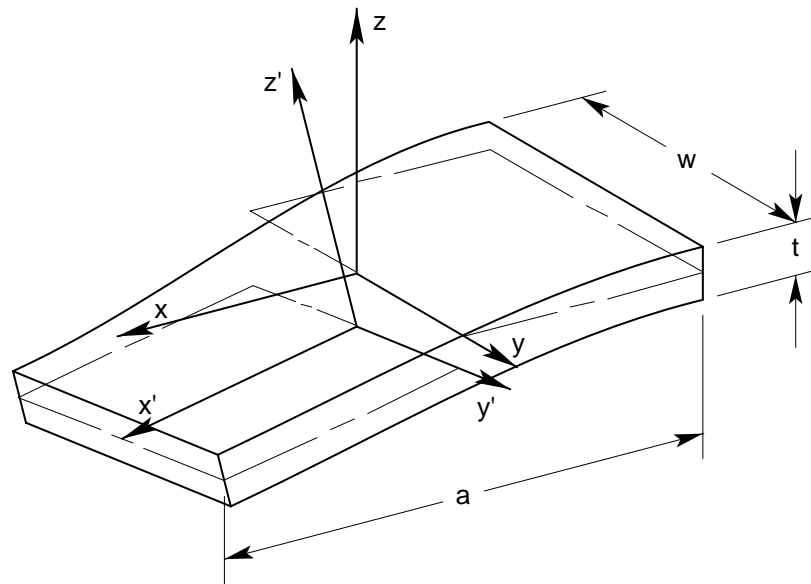
Figure 6-27 Imagining the CS's as rigid links to the ends of the blade, the application of forces and moments at these CS's results in respective displacements and rotations with no coupling between axes.

The flexion of a blade may be represented as movement between two CS's that attach to opposite ends of the blade. It would be more common to place a CS at each end but it is more convenient to place them initially coincident with the principal axes of the blade. Then a blade undergoing flexion appears as slightly displaced CS's in Figure 6-27. In similar fashion, the forces and moments may be represented about these CS's rather than at the ends where they are physically applied. This choice of CS's diagonalizes the compliance

matrix. Four of the six diagonal elements appear already in Chapter 2.6 as stiffnesses but without derivation or explanation. Here we go through each element with due care and add more generality with column effects and side-by-side blades. As in Figure 6-26, w_2 is the outside dimension of blades and w_1 is the inside dimension. In addition, it is necessary to represent the width of the individual blades or of a single blade as w.

We begin with the in-plane constraint directions. Axial compliance is the first diagonal element in the compliance matrix (6.19) and is so familiar that it needs no explanation. It is linear in all the key parameters and therefore is convenient for normalizing the other compliances. The second diagonal element (6.20) corresponds to a y-direction force, which produces combined bending and shear in the blade. It comes from the familiar fixed-guided beam equation and has an added term for the shear deformation. The section properties have been simplified for the side-by-side blade geometry. The last constraint direction is also the last element in the compliance matrix (6.21). Here the blade is in pure bending due to a moment about the z axis.

$$\mathbf{C}_{1,1} = c_x = \frac{a}{E\,t\left(w_2 - w_1\right)} \tag{6.19}$$

$$\mathbf{C}_{2,2} = c_y = c_x\left\{\frac{a^2}{w_1^{\,2} + w_1\,w_2 + w_2^{\,2}} + 2.4\left(1 + \nu\right)\right\} \tag{6.20}$$

$$\mathbf{C}_{6,6} = c_{\theta_z} = \frac{12\,c_x}{w_1^{\,2} + w_1\,w_2 + w_2^{\,2}} \tag{6.21}$$

The remaining diagonal elements are out-of-plane directions usually considered as degrees of freedom. The elements corresponding to z and θ_y directions are similar to y and θ_z directions from before and differ mainly in a factor t^2 in the denominator rather than w^2. However, there are two subtle distinctions. As noted earlier in Section 6.2.2, the equations for bending compliance should include a factor $(1 - \nu^2)$ to account for the Poisson effect. The other factor is the effect of an axial force, either compressive or tensile. The solutions for fixed-guided and cantilever boundary conditions are available from numerous sources, for example, [Vukobratovich and Richard, 1988], [Young, 1989] and [Smith, 1998]. Unfortunately the equations are not particularly convenient or intuitive, involving trigonometric functions for compression and hyperbolic functions for tension. Upon substituting power series approximations, the two types of functions become the same when expressed with a positive or negative axial force. The number of terms required in the power series depends upon how closely the flexure operates to the critical buckling load. We will keep enough terms to have good accuracy through one-half the critical load.

The third diagonal element for the z-direction force (6.22) follows from the series approximation of the axially loaded, fixed-guided beam. The effect of the axial force is contained within the square brackets. As expected, the compliance decreases for a positive

tensile force and increases for a negative compressive force. The approximation differs from the exact solution by only 6.6% at one-half the critical load. Usually we would not venture this close to buckling unless the intent is a zero-stiffness condition. Then it is necessary to use the exact solution from the references.

$$\mathbf{C}_{3,3} = c_z \cong c_x \left\{ \left(1 - v^2\right) \left(\frac{a}{t}\right)^2 \left[1 - \frac{6}{5}\gamma + \frac{17}{35}\gamma^2 - \frac{62}{315}\gamma^3\right] + 2.4\left(1 + v\right) \right\}$$

(6.22)

$$\gamma \equiv \frac{f_x c_x a}{t^2} \qquad \gamma_{cr} = \frac{\pi^2}{12}$$

The fifth diagonal element corresponds to a moment load applied about the y-axis. When an axial force also exists, we must be careful to apply it through the CS rather than at the end of a cantilever beam as in the published solution. Figure 6-28 shows the subtle difference in the way the axial force is applied to the end in (a) and through the CS in (b). The differential equation for the model in (b) has one additional term, $f \theta$ (a - x). The solution proceeds in a similar way and simplifies for compression to a single sine function rather than a tangent function or the equivalent hyperbolic function for tension. Applying the series approximation results in the fifth diagonal element (6.23). In this case the compliance increases under tension and decreases under compression.
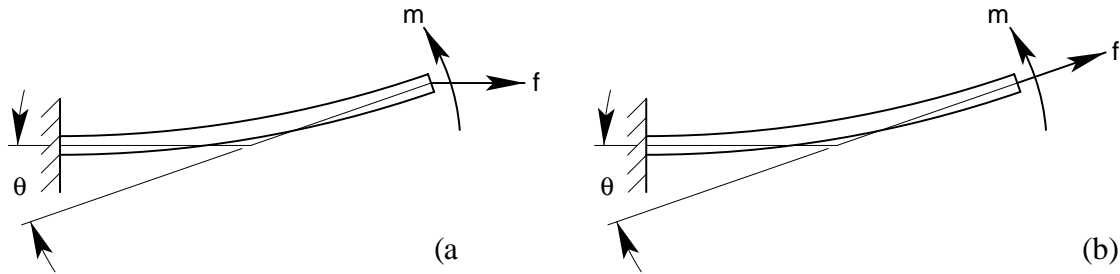
Figure 6-28 The tensile force stiffens the beam in (a) while making it more compliant in (b).

$$\mathbf{C}_{5,5} = c_{\theta_y} = \frac{12\, c_x}{t^2}\left(1 - v^2\right)\left[1 + 2\gamma + \frac{6}{5}\gamma^2 + \frac{12}{35}\gamma^3\right]$$

(6.23)

The fourth diagonal element (6.24) corresponds to twisting of the blade. This relation comes from the parallel combination of two effects. The first term within the braces is simple twist with no end effects. This solution is given in several references, for example, [Timoshenko and Goodier, 1951] and [Young, 1989]. The second term brings in the end effects by considering the blade as a series of thin fixed-guided beams distributed across the width. The deflection varies as the radius from the twist axis, and an integration provides the cumulative effect. Since c_z appear in this relationship, it accounts for the Poisson and axial-force effects. This relation agrees well with a parameterized finite-element study.

$$\mathbf{C}_{4,4} = c_{\theta_x} = 12 \left\{ \frac{1}{2(1+v)} \left(4 + 2.52 \frac{t}{w} \right) \frac{t^2}{c_x} + \frac{w_1^2 + w_1 w_2 + w_2^2}{c_z} \right\}^{-1} \tag{6.24}$$

6.2.5.2 The Stress Matrix for a Blade Flexure

The distribution of stress through a blade varies greatly depending on the direction of the applied force or moment. For purposes of sizing the blade, however, it is sufficient to consider only the maximum absolute value of stress resulting from applied forces and moments. This information may be represented in a diagonal matrix similar to the compliance matrix. The judicious choice of the CS causes symmetric distributions of stress due to individual components of the force-moment vector. Each distribution will have the maximum absolute value of stress always extending to the eight corners of the blade. There is one worse-case corner where all the stresses are in general alignment (perfectly aligned if not for shear stresses). Then a somewhat conservative estimate of the combined maximum absolute principle stress is the simple sum of the individual maximum's as calculated from the stress matrix multiplied by the applied force-moment vector.

In keeping with the order presented for the compliance matrix, the three terms that correspond to constraint directions are considered first for the stress matrix. The first diagonal element for axial loading (6.25) is simply the inverse of the cross sectional area. It is convenient to use for scaling the other terms. For the second diagonal element (6.26), the y-direction force produces combined bending and shear in the blade. A somewhat conservative approach treats the maximum absolute value of principle stress as if aligned with the x-axis. This simplifies the final step of combining all the stress components but yields a slightly higher combined stress than a more rigorous analysis. The last constraint direction and also the last element in the stress matrix (6.27) is much simpler because the blade is in pure bending from a z moment.

$$\mathbf{S}_{1,1} = s_x = \frac{1}{t(w_2 - w_1)} \tag{6.25}$$

$$\mathbf{S}_{2,2} = s_y = s_x \left\{ \frac{3 a w_2}{2(w_1^2 + w_1 w_2 + w_2^2)} + \sqrt{\left(\frac{3 a w_2}{2(w_1^2 + w_1 w_2 + w_2^2)} \right)^2 + 1} \right\} \tag{6.26}$$

$$\mathbf{S}_{6,6} = s_{\theta_z} = s_x \frac{6 w_2}{w_1^2 + w_1 w_2 + w_2^2} \tag{6.27}$$

The stresses due to the remaining three elements usually result due to required motions of the flexure but they will be written for applied loads. The third diagonal element (6.28) corresponds to a z-direction force. Although the blade experiences combined bending and shear loading, the shear stress is usually not significant given normal blade

201

proportions. It is excluded in preference of keeping a simple expression for the column effect from an axial force. As expected the bending stress increases with a negative compressive force and decreases with a positive tensile force. The fifth diagonal element corresponds to a *y*-moment (6.29) and exhibits slightly more complicated behavior. The axial force causes the bending moment to be nonsymmetric along the length of the blade.[I] The bending moment is maximum at the fixed end for tension and minimum for compression. The use of the singularity function in the equation turns off the effect of a compressive force when γ is negative, leaving just the applied moment as the maximum.

$$\mathbf{S}_{3,3} = s_z = s_x \frac{3a}{t}\left[1 - \gamma + \frac{6}{5}\gamma^2 - \frac{51}{35}\gamma^3\right] \tag{6.28}$$

$$\mathbf{S}_{5,5} = s_{\theta_y} = s_x \frac{6}{t}\left[1 + 6\langle\gamma\rangle^1 + 6\langle\gamma\rangle^2 + \frac{12}{5}\langle\gamma\rangle^3\right] \tag{6.29}$$

As described in the previous section, there are two effects to consider when a blade twists on axis. The first is simple twist with no end effects. The shear stress produced is maximum far away from the corners and therefore may be safely ignored. The other effect is bending of the blade as a fixed-guided beam with the maximum stress occuring at the corners. The fourth diagonal element (6.30) represents this effect by using s_z as the reference rather than s_x. As a result it also represents column effects.

$$\mathbf{S}_{4,4} = s_{\theta_x} = s_z \frac{6\,w_2}{w_1{}^2 + w_1\,w_2 + w_2{}^2} \tag{6.30}$$

The stress matrix multiplied by the force-moment vector gives a vector of stress components that may be positive or negative depending on the loading. It is useful to look at each component to understand which loads are most significant. The worse-case stress is conservatively estimated by summing the absolute values of the stress components.

6.2.5.3 Parallel-Series Spring Models

The use of parallel and series combinations of springs is fairly common in engineering analysis. Working in 6-D is certainly less common but the basic concept of parallel-series combinations is no different. Most of the gritty details are in the matrix algebra carried out by the computer. The most challenging aspect usually is in setting up the transformation matrices. Perhaps the best way to understand the modeling aspect is to work through an example step by step. The X-Y-θ_z flexure stage, shown in Figure 6-11 on page 184, is a good example to represent several levels of parallel and series combinations of springs.

[I] The asymmetry of the bending moment is a consequence of the way the blade is loaded along the *x* axis of one CS. A symmetric bending moment would result if the axial force bisected the *x* axes of both CS's. This symmetric case is more appropriate for the cross blade flexure but not for more general arrangements.

Figure 6-29 shows the spring model of the same flexure stage with three actuators. The steps required to set up and analyze the model are enumerated below.
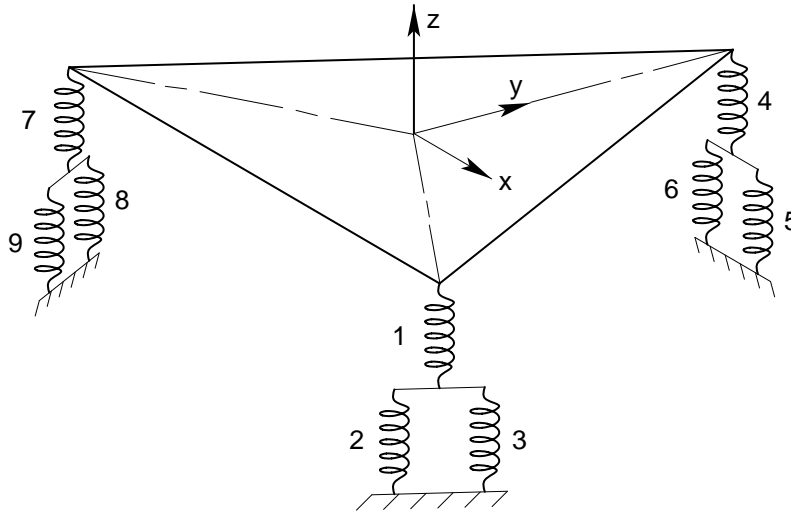
Figure 6-29 The X-Y-θ_Z flexure stage appearing in Figure 6-11 is modeled with nine springs in parallel and series combinations as shown.

a) Identify the main member (the thing being moved or supported) and attach the base coordinate system CS_0 at a convenient location. It is simple to reflect the results to a different CS if desired.

b) Identify all the separate paths from the main member to ground. There are six in the example, three flexure supports and three actuators.

c) Identify and number each spring in each path. There are nine in the example, six blades and three actuators.

d) Assign a unique CS to each spring. Number these CS_1 to CS_n. Then create [6 x 6] transformation matrices to represent the spatial relationships between the local CS's and the base CS_0.

e) Create as many compliance matrices as required to represent all the springs with respect to their own local CS's. There are only two for the example, one matrix for six identical blades and one matrix for three identical actuators.

f) Reflect the compliance matrix for each spring to the base CS_0 using the transformation matrices, thus creating n unique compliance matrices. Number these $\mathbf{C}_1$ to $\mathbf{C}_n$.

g) Identify the springs that form either series or parallel combinations. When reflected to the same CS, series springs experience the same load while parallel springs experience the same deflection. The example has three sets of parallel springs, 2-3, 5-6 and 8-9.

h) Add the stiffness matrices of springs in parallel and add the compliance matrices of springs in series. Indicate these new equivalent springs by the spring numbers they represent. The equivalent springs for the example are $\mathbf{K}_{2\text{-}3}$, $\mathbf{K}_{5\text{-}6}$, and $\mathbf{K}_{8\text{-}9}$.

i) Repeat steps 7 and 8 using the equivalent springs in place of the ones they represent. Stop when there is only one equivalent spring remaining. The example requires a total of three combination steps before reaching the equivalent spring for the system. The second step is a series combination resulting in $\mathbf{C}_{1\text{-}2\text{-}3}$, $\mathbf{C}_{4\text{-}5\text{-}6}$, and $\mathbf{C}_{7\text{-}8\text{-}9}$. The last step is a parallel combination resulting in $\mathbf{K}_0$, the equivalent spring for the system.

There are a number of uses for the system stiffness and compliance matrices. Presumably there is some requirement that drives the design to have a certain level of stiffness in the constraint directions and certain freedoms in other directions. Specific load cases may be applied to ascertain deflections or certain motions may be specified to determine resulting reaction forces. The sizes and locations of blades are easily modified to evaluate design changes. Details about individual blades such as stresses or reaction forces require the applied load or specified motion to be propagated back through the combination process, being careful to apply loads to springs in series or motions to springs in parallel. A clearly labeled sketch of the model for each step in the combination process will help avoid confusion and mistakes.

The fine details of these analysis steps appear in the flexure system analysis program in Section 6.3. The program documents the example of the X-Y-θ_z flexure stage discussed here. In particular it shows how to set up the [6 x 6] transformation matrices and reflect compliance matrices to the base CS_0. It also shows how easily a fairly complex system of blades is modeled with parallel and series combinations of springs.

A slightly more advanced topic is the modeling of column effects in a system of flexures. It was not an important effect in the X-Y-θ_z flexure stage so it was not introduced then. The compliance matrix and the stress matrix for individual blades account for local column effects, but it is necessary to include the system effects at the system level. Fortunately this is straightforward to do with additional springs that represent the column behavior. This behavior may occur when a series combination carries a significant axial force, for example, when two blades lie in the same plane so as to act like one much longer blade. The effect of the axial force is modeled with a new spring placed in parallel with the series combination. The stiffness of the new spring depends only on the axial force and the distance between the two CS's of the series combination, as in Equation 6.31. It may be positive or negative for a tensile or compressive force, respectively. When reflecting this stiffness to the base CS_0, the transformation matrix should be the same as the most mobile blade in the series combination. Then it may be combined as any of the other springs.

$$\mathbf{K}_{3,3} = \frac{f_x}{L} \tag{6.31}$$

6.3 Friction-Based Design of Kinematic Couplings[I]

Friction affects several aspects important to the design of kinematic couplings, but particularly the ability to reach the centered position is fundamental. It becomes centered when all constraints are fully engaged even though a small uncertainty may exist about the ideal center where potential energy is minimum. For many applications, centering ability is a good indicator for optimizing the coupling design. Typically, the coupling design process has been largely heuristic based on a few guidelines [Slocum, 1992]. Symmetric forms of the basic kinematic couplings are simple enough to develop closed-form equations for centering ability. More general configurations lacking obvious symmetries are difficult to model in this way. A unique kinematic coupling for large, interchangeable optics assemblies in the NIF motivated the development of computer software to optimize centering ability. The program, written in Mathcad™ Plus 6, appears in Section 6.3.

6.3.1 Friction Effects in Kinematic Couplings

Friction affects at least four important characteristics of a kinematic coupling as indicated by order-of-magnitude estimates that all include the coefficient of friction μ. These estimates are listed in Equations 6.32 through 6.35 and are described below.

Repeatability
$$\frac{f}{k} \approx \mu \left(\frac{2}{3R} \right)^{1/3} \left(\frac{P}{E} \right)^{2/3} \qquad (6.32)$$

Kinematic support
$$\left| f_t \right| \leq \mu \, f_n \qquad (6.33)$$

Stiffness
$$k_t = k_n \frac{2 - 2\nu}{2 - \nu} \left(1 - \frac{f_t}{\mu \, f_n} \right)^{1/3} \approx 0.83 \, k_n \qquad (6.34)$$

Centering ability
$$\frac{f_c}{f_n} \approx 0.5 - 1.3\mu \qquad (6.35)$$

Tangential friction forces at the contacting surfaces may vary in direction and magnitude depending how the coupling comes into engagement. This affects the repeatability of the coupling and the kinematic support of the precision component. The estimate for repeatability is the unreleased frictional force multiplied by the coupling's compliance. The estimate is derived as if the coupling's compliance in all directions is equal to a single Hertzian contact carrying a load P and having a relative radius R and elastic modulus E. The frictional force acts to hold the coupling off center in proportion to the compliance. This estimate will underestimate the repeatability if the structure of the coupling is relatively compliant compared to the contacting surfaces.

[I] This material was previously published in condensed form [Hale, 1998].

Kinematic support is important for stability of shape of the precision component being supported by the coupling. The estimate for kinematic support simply gives a bound on the magnitude of friction force acting at any contact surface. A sensitivity analysis of the precision component will determine a tolerable level of friction that the coupling can have. This may drive the design to include flexure elements and/or procedures to release stored energy. If repeatable engagement is not so important, then constraints using rolling-element bearings offer very low friction. For example, a pair of cam followers that contact with crossed axes is equivalent to a sphere on a flat but with twenty or more times less friction.

In some cases frictional overconstraint is valuable for increasing the overall system stiffness. Provided the tangential force is well below what would initiate sliding, the tangential stiffness of a Hertzian contact is comparable to the normal stiffness [Johnson, 1985]. This motivated the widely spaced vee used to stiffen the first torsional mode of NIF optics assemblies (see Figure 6-9).

Centering ability can be expressed as the ratio of centering force to nesting force. The estimate provided is typical for a symmetric three-vee coupling. A larger ratio means the coupling is better at centering in the presence of friction. It is also convenient to express centering ability as the coefficient of friction where this ratio goes to zero. For the estimate, the limiting coefficient of friction is $0.5/1.3 = 0.38$. The coupling will center if the real coefficient of friction is less than the limiting value.

6.3.2 Centering Ability of the Basic Kinematic Couplings

We begin by studying the centering ability of the basic kinematic couplings because their geometry is relatively simple and familiar. When brought together initially off center, the constraints engage sequentially as the coupling seeks a path to center.[I] This path becomes better defined as more constraints engage. For example, five constraints allow the coupling to slide along one well-defined path. Four constraints allow motion over a two-dimensional surface of paths and so forth. Although there are infinitely many paths to center, only the limiting case is of practical interest for determining centering ability. Further, it is reasonable to expect the limiting case to be one of six possible paths that have five constraints engaged.[II] This point will be demonstrated using examples and simple logic.

The simplest example is the symmetric three-vee coupling. Figure 6-30 shows two ways that the coupling may slide to center depending on its initial misalignment. In (a), two vee constraints are fully engaged and the third is off center giving a total of five constraints. The two vees define an instantaneous center of rotation. The off-center vee transforms its share (one-third) of the nesting force into a centering moment about the instant center.

[I] It is a rare possibility that initial contact can occur at two places simultaneously.
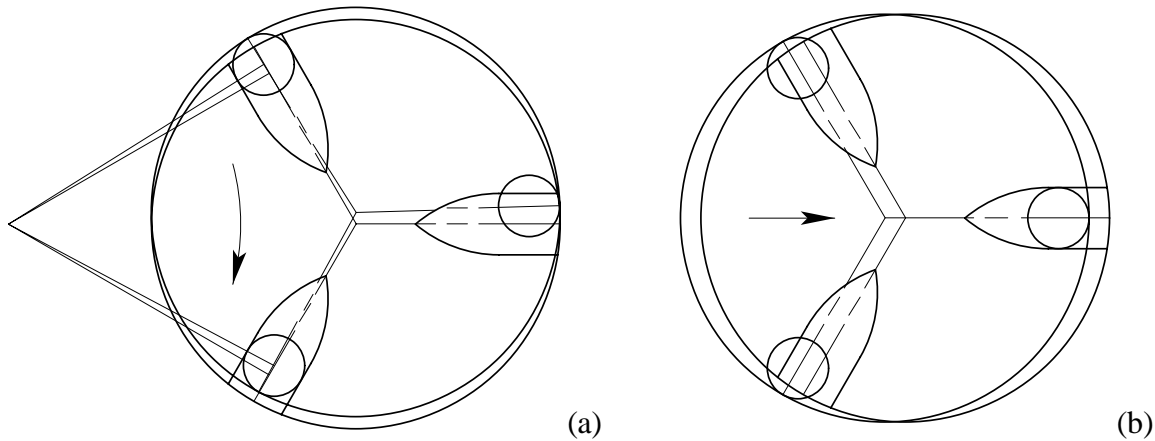
[II] The exception to this statement is the ball-cone constraint since the cone provides only one constraint until the ball is fully seated. A tetrahedral socket remedies this situation.

Equation 6.36 describes the centering force at the center of the coupling due to this moment, where α is the angle to each surface from the plane of the vees. This path is the limiting case along with five other symmetrically identical paths.[I] In (b), two off-center vees transform their share (two-thirds) of the nesting force into a centering force given by Equation 6.37. This causes the coupling to translate along the fully engaged vee. With only four constraints, the coupling is also free to roll but there is no moment in this direction. Given freedom like this, the coupling will move in the general direction of the centering force until the next constraint engages and forces it along a more resistive path to center.

$$\frac{f_c}{f_n} = \frac{\sin\alpha - \mu\cos\alpha}{2(\cos\alpha + \mu\sin\alpha)} - \frac{\sqrt{3}\,\mu}{3\cos\alpha} \tag{6.36}$$

$$\frac{f_c}{f_n} = \frac{\sqrt{3}\,\sin\alpha\,\sqrt{4 + 3\tan^2\alpha} - 4\mu}{3\left(\cos\alpha\,\sqrt{4 + 3\tan^2\alpha} + \sqrt{3}\,\mu\,\tan\alpha\right)} - \frac{\mu}{3\cos\alpha} \tag{6.37}$$

(a)   (b)

Figure 6-30 In (a), the three-vee coupling slides on five constraints producing rotation about an instant center. In (b), the coupling slides on four constraints in the general direction of the centering force.

The three-tooth coupling behaves similarly to the three-vee coupling, but the centering force with five constraints engaged is very difficult to model in closed form. Table 6-1 shows the limiting coefficient of friction for both three-vee and three-tooth couplings as calculated by the kinematic coupling analysis program. There is negligible difference between the two types over the range 45° to 55°. The three-vee coupling has slightly better centering ability at the nearly optimal angle of 60°. With only four constraints engaged, the centering force causes simple translation of the three-tooth coupling, which leads to a reasonable closed-form solution given by Equation 6.38. Graphs of Equations 6.36, 6.37 and 6.38 versus the coefficient of friction μ appear in Figure 6-32 (a). The point to notice is that the centering force decreases when the fifth constraint engages.

[I] The coupling may rotate clockwise or counterclockwise about any of three instant centers.

Angle of Inclination α	45°	50°	55°	60°	65°
Three-Vee Coupling	0.317	0.338	0.354	0.364	0.365
Three-Tooth Coupling	0.319	0.339	0.351	0.352	0.339

Table 6-1 The limiting coefficient of friction versus angle for three-vee and three-tooth couplings.

$$\frac{f_c}{f_n} = \frac{\sin\alpha\,\sqrt{4+\tan^2\alpha}-4\mu}{2\left(\cos\alpha\,\sqrt{4+\tan^2\alpha}+\mu\tan\alpha\right)} \tag{6.38}$$

An aspect hidden by the symmetry in the previous examples is the possibility that a path with five constraints engaged may have greater centering force than a different path with only four constraints. However as the coupling continues toward center, the centering force cannot increase as the fifth constraint engages. The tetrahedron-vee-flat coupling exhibits behavior of the type shown in Figure 6-32 (b). Usually the centering ability will be limited by the path shown in Figure 6-31 (a). The centering force for this path is given in Equation 6.39, where α is the vee angle and β is the tetrahedron angle. The opposite-direction path has one less constraint and greater centering force as described by Equation 6.40. This solution is also representative of the cone-vee-flat coupling. However in Figure 6-31 (b), a different path with five constraints has typically greater centering force as described by Equation 6.41. The main point is that all six paths having five constraints engaged must be considered to determine centering ability.

(a)   (b)
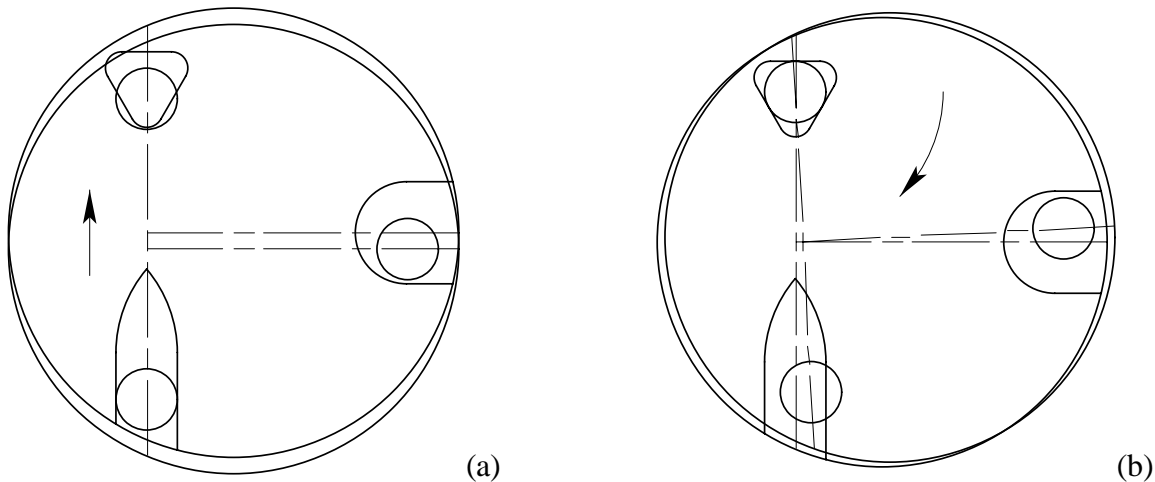
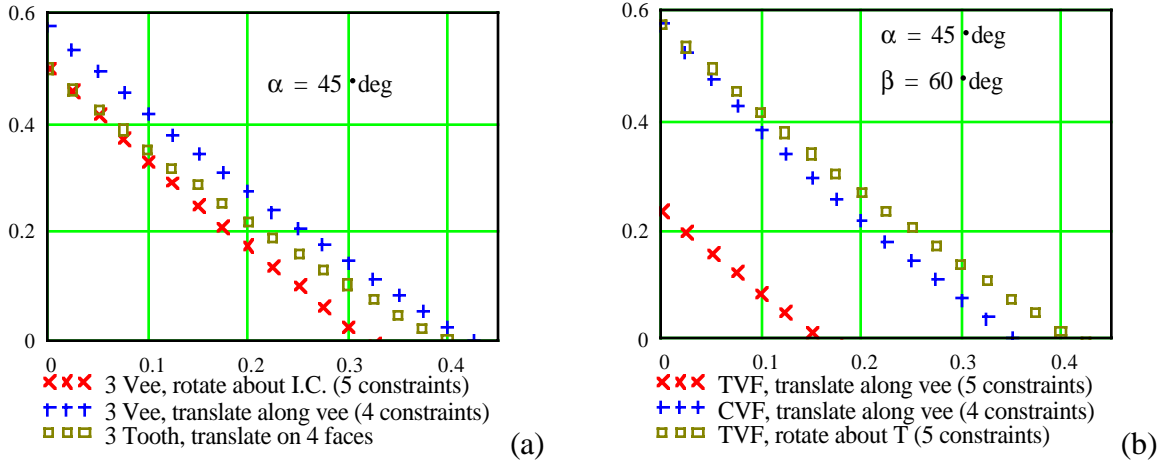**Figure 6-31** The tetrahedron-vee-flat coupling has six unique paths having five constraints engaged. The path in (a) usually limits the centering ability of the coupling. The path in (b) could limit the centering ability if the vee angle is too shallow.

$$\frac{f_c}{f_n} = \frac{\sin\beta\,\sqrt{4+\tan^2\beta}-4\mu}{6\left(\cos\beta\,\sqrt{4+\tan^2\beta}+\mu\tan\beta\right)} - \frac{\mu}{3\cos\alpha} - \frac{\mu}{3} \tag{6.39}$$

$$\frac{f_c}{f_n} = \frac{\sin\beta - \mu\cos\beta}{3(\cos\beta + \mu\sin\beta)} - \frac{\mu}{3\cos\alpha} - \frac{\mu}{3} \tag{6.40}$$

$$\frac{f_c}{f_n} = \frac{\sqrt{3}}{3}\left\{\frac{\sin\alpha - \mu\cos\alpha}{\cos\alpha + \mu\sin\alpha} - \mu\right\} \tag{6.41}$$

Figure 6-32 Normalized centering force versus coefficient of friction. In (a), the three-vee and three-tooth couplings being symmetric always have five-constraint paths with less centering force than all four-constraint paths. In (b), the tetrahedron-vee-flat coupling may have five-constraint paths with more centering force than some four-constraint paths.

The difficulty encountered with more general configurations of kinematic couplings comes first in determining the six possible paths to center then in developing compatibility and equilibrium equations for complex geometry. Even when the coupling has relatively simple geometry, the equations are rather tedious to develop. Compound this with the problem of optimizing the design and it becomes obvious that a systematic, computer-based approach is essential for designing more general configurations of kinematic couplings.

6.3.3 A General Approach for Optimizing Centering Ability

There are three basic steps required for optimizing the ability of a kinematic coupling to become centered.

- Represent the geometric arrangement of six constraints with model parameters. Some parameters will vary during the optimization while others may be fixed by strict design constraints. This step requires user knowledge and input following the general format provided by the program.

- Determine the six paths to center and the coefficient of friction for each path that just impedes sliding (i.e., zero centering force). This step is purely algorithmic.

- Vary the model parameters to maximize the minimum coefficient of friction among the six paths. This step could be strictly algorithmic but experience has shown the user's

intelligence to be very valuable. Keeping the user in the loop builds intuition and understanding of the tradeoffs involved.

These three steps are explained through the example that motivated this work, the NIF optics assembly.

Orthographic and isometric views of one NIF optics assembly, discussed previously in Section 6.1.3.3 and again in Chapter 7, appear in Figure 6-33. The six constraints that kinematically support the optics assembly are represented in the figure by reaction force vectors numbered 1 to 6. In the model, each constraint is represented by a simple spring stiffness defined along the *z*-axis of a local *x-y-z* coordinate system (CS). The use of six-dimensional vectors and [6 x 6] transformation matrices completely automates the development of compatibility and equilibrium equations, but the local CS's can be challenging to set up even for experienced users. See Appendix A for a complete discussion of transformation matrices.

In the program, two equations completely define the local CS's for any arrangement of six constraints. Equation 6.42 defines the overall transformation matrix as a series of simple transformations: *x-y-z* translation, *z* rotation, *y* rotation and *x* rotation. The user must decide the proper number and order of simple transformations for the application, but usually there will be six parameters, p_1 through p_6. These parameters come from the column of Equation 6.43 that corresponds to the particular constraint under consideration. In the example, the CS definition for constraint 1 is: rotate θ_2 about global *x*, rotate $-\theta_1$ about global *y*, and translate in global *x-y-z* (-0.385, -0.315, -0.8). An equivalent definition is: translate in local (initially global) *x-y-z* (-0.385, -0.315, -0.8), rotate $-\theta_1$ about local *y*, and rotate θ_2 about local *x*. During the optimization, constraints 1 and 3 symmetrically change orientation according to θ_1 and θ_2. Similarly, constraints 2 and 4 change according to θ_1 and θ_3, and constraints 5 and 6 change according to θ_4. The user determines the number of variable parameters used in the optimization. In addition, the user must supply the nesting force vector and a vector of spring stiffnesses, one for each constraint.

$$T(p) := T_{xyz}(p_1, p_2, p_3) \cdot R_z(p_6) \cdot R_y(p_5) \cdot R_x(p_4)$$
(6.42)

$$P(\theta) := \begin{bmatrix} -0.385 & -0.385 & 0.385 & 0.385 & -0.397 & 0.397 \\ -0.315 & -0.315 & -0.315 & -0.315 & -0.241 & -0.241 \\ -0.8 & -0.8 & -0.8 & -0.8 & 0.85 & 1.31 \\ \theta_2 & -\theta_3 & \theta_2 & -\theta_3 & 90 \cdot \deg & 90 \cdot \deg \\ -\theta_1 & -\theta_1 & \theta_1 & \theta_1 & 0 & 0 \\ 0 & 0 & 0 & 0 & -\theta_4 & \theta_4 \end{bmatrix}$$
(6.43)
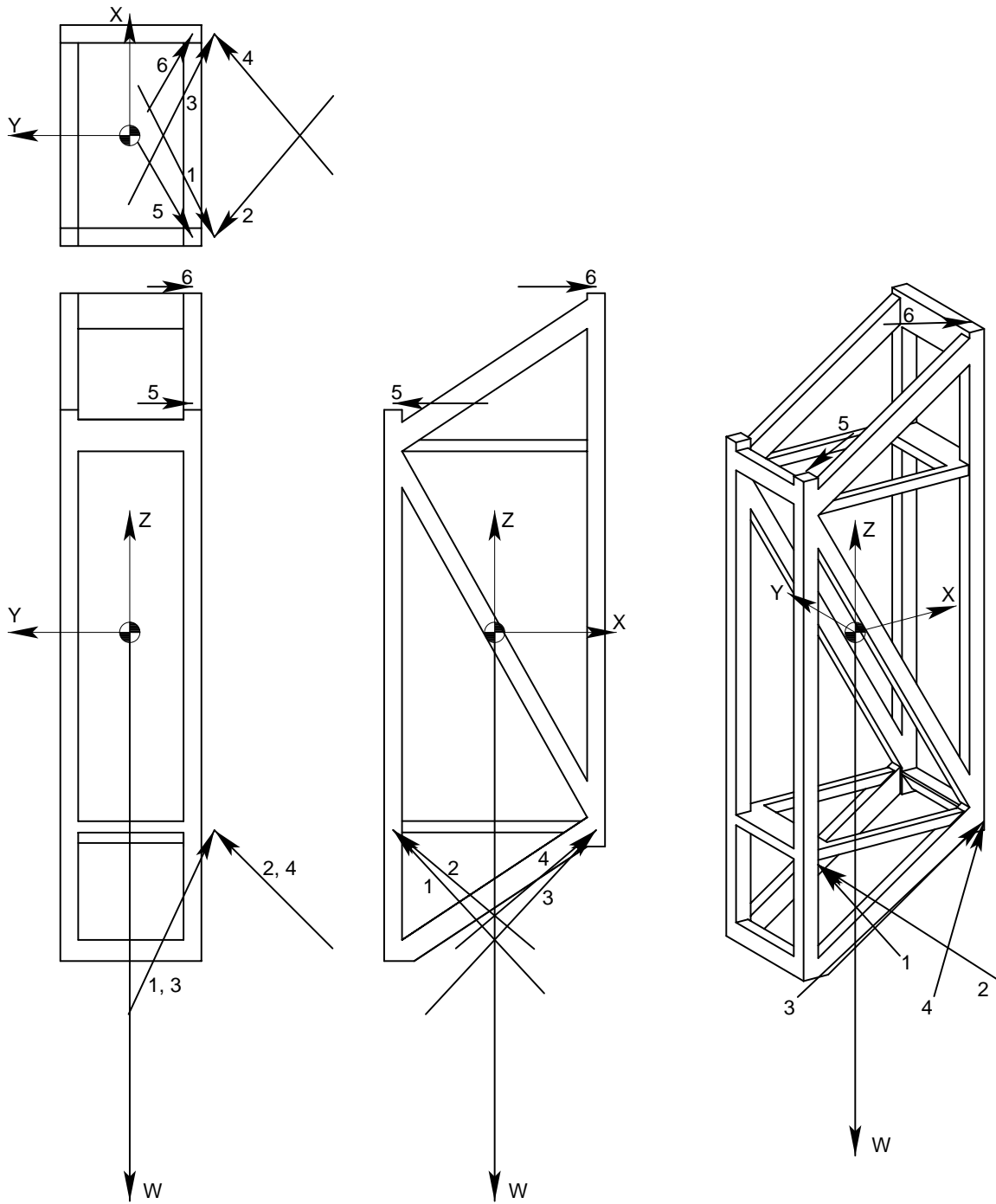
Figure 6-33 Orthographic and isometric views of one NIF optics assembly. The arrows numbered 1-6 represent the six constraints that support the assembly. The arrows are proportional to the reaction forces.

The second step uses the constraint arrangement, the nesting force vector and constraint stiffnesses to determine the six paths to center and the coefficient of friction for each path that yields zero centering force. If the constraint arrangement is truly kinematic, then the parallel combination of six constraint stiffnesses will form a [6 x 6] stiffness matrix for the coupling that is full rank. Equation 6.17 (also A.35) on page 198 expresses the

process of reflecting the stiffness matrix from a local CS_i to a global CS_0 then summing all the reflected stiffness matrices. Since there is only one nonzero term in $\mathbf{K}_i$, the matrix equation reduces to an outer product of the third column of $\mathbf{T}_{0/i}$ times the simple stiffness.

The technique used to find the vector direction for sliding is rather elegant. A degenerate stiffness matrix is computed for only five constraints engaged. This matrix has five nonzero eigenvalues (if the coupling is truly kinematic). The eigenvector corresponding to the zero eigenvalue gives the direction in the global CS that the coupling will slide for that particular set of five constraints. This procedure is executed six times, once for each constraint <u>not</u> engaged.

The procedure used to determine the coefficient of friction for zero centering force is coded in just three expressions but becomes rather complicated to explain. It should help to review the comments and equations in the program. Starting with one sliding vector in the global CS, the same transformation matrices are used to create six local sliding vectors, one for each constraint. Then a six-dimensional, force-moment vector is calculated for each constraint using the Coulomb law of friction and a unit normal force. Transforming back to the global CS, the vectors are assembled into a matrix that when multiplied by a vector of normal forces (i.e., the contact force for each constraint) gives the resultant force-moment vector for the coupling. The inverse of this matrix is useful because it takes the applied force-moment vector (i.e., the nesting force) and gives back the contact forces for a given coefficient of friction. Finally, the row of this matrix equation corresponding to the constraint not engaged is solved for the coefficient of friction that makes its normal force zero. This gives the coefficient of friction that just impedes sliding. This procedure is executed six times, once for each constraint not engaged. The minimum of six results is the limiting coefficient of friction for the particular constraint arrangement.

The last step is to adjust the constraint arrangement in a manner that maximizes the limiting coefficient of friction. The user presumably has set up the program to include some number of variable parameters given by the vector θ. The optimization approach is a graphical technique that provides the user with sufficient visual feedback to find the optimum within a few iterations. The user must enter three vectors: the nominal vector θ and the range for the graph, θ_{min} and θ_{max}. For each parameter, the program generates one curve over its range while holding all other parameters at their nominal values. All curves appear in one graph versus a normalized range of model parameters. The user adjusts the nominal values attempting to maximize the limiting coefficient of friction.

Figure 6-34 shows two graphs for the NIF optics assembly with slightly different nominal parameters. The horizontal dashed line indicates the limiting coefficient of friction for the nominal parameter set. The optimal parameter set is apparent in (a) because a change to any one parameter reduces the limiting coefficient of friction. It is useful to observe the suboptimal parameter set in (b). By adjusting the nominal values towards the peaks in the curves, the user soon converges to the optimal parameter set.
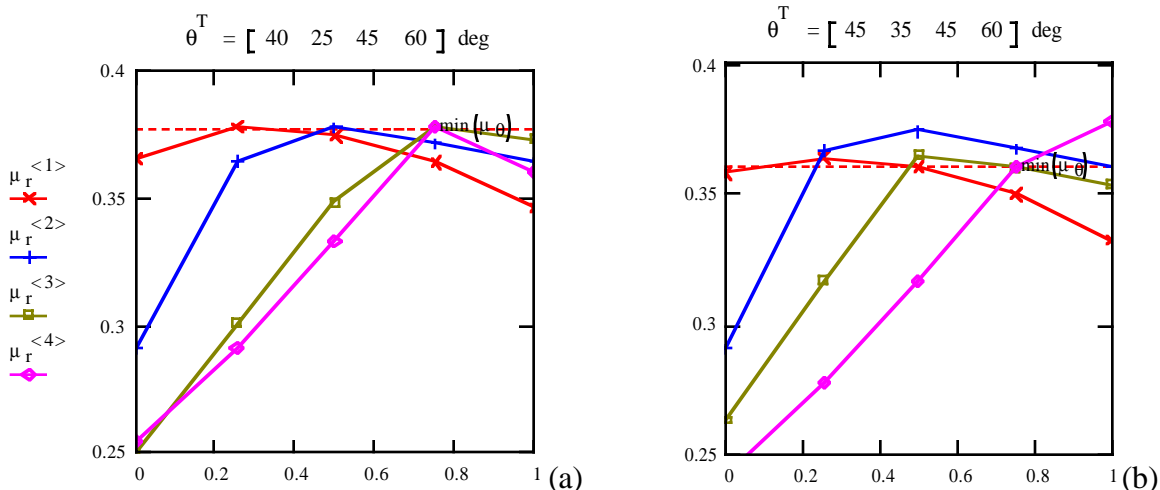
Figure 6-34 Limiting coefficient of friction versus a normalized range of model parameters. Each curve corresponds to one individually varying parameter with the others held constant at nominal values. The horizontal dashed line indicates the nominal parameter set. The graph in (a) shows the optimal configuration while (b) is suboptimal. In this example, the markers occur in 5° increments of the angle parameters.

6.4 Mathcad™ Documents for Generalized Kinematic Modeling

The Mathcad computing environment is ideal for engineering analysis where it is important for the user to understand the mechanics of the program. All the code is in plain sight and in familiar mathematical format. It is easy to add text and drawings to better explain how to use the program, usually referred to as a document.

6.4.1 Flexure System Analysis Program

This program helps the user develop a parameterized model of a flexure system so that sizes and locations of blades may be chosen to achieve key performance requirements. Each blade in the system is represented by the compliance matrix of a spring in a local coordinate system (CS). All blades are then reflected to a common CS to allow simple addition of compliance matrices for springs in series or of stiffness matrices for springs in parallel. The end result is the equivalent compliance matrix for the system and its reciprocal, the stiffness matrix. Applied loads or specified motions may then be applied to these matrices to determine the resulting behavior. Loads may be propagated back to local blades to determine the maximum stresses.

This program uses six dimensional vectors and [6 x 6] matrices to deal simultaneously with both linear and angular measures. The first three components correspond to linear measures such as force and displacement, and the last three correspond to angular measures such as moment and rotation. The same arrangement applies to the rows and columns of the matrices used for coordinate transformation, stiffness and compliance. In addition, the positions and orientations for an arbitrary number n of flexure blades are conveniently stored in an [m x n] matrix. Each column describes a sequence of moves (typically m = 6) required to go from the global X-Y-Z CS to a local x-y-z CS as shown in the figure. This matrix may also contain parameters that the user may vary to optimize the configuration.

Forces and displacements for the flexure system are represented in the global CS while forces and displacements at a particular flexure are represented in its local x-y-z CS.

The transformations between the X-Y-Z CS and x-y-z CS's are done as a sequence of moves. The number and order may vary to suit the application, but they must be the same for each flexure since they are stored in a matrix. The basic moves are: translation in x-y-z, rotation about x, rotation about y and rotation about z. The sequence may be interpreted as moves relative to the base CS or in the opposite order as moves relative to the local CS. Two rules express these interpretations for a sequence of transformation matrices: 1) post multiply to transform in the local CS and 2) pre multiply to transform in the base CS. A typical sequence relative to the base CS is: rotate about the X axis, rotate about the Y axis, rotate about the Z axis, and translate (X, Y, Z). The equivalent sequence relative to the local CS is: translate (x, y, z) (initially coincident with the base CS), rotate about the z axis, rotate about the y axis, and rotate about the x axis. The transformation matrix for this sequence is $T_{XYZ} R_Z R_Y R_X$.

Enter each blade parameter in a row vector with as many columns as unique blades.
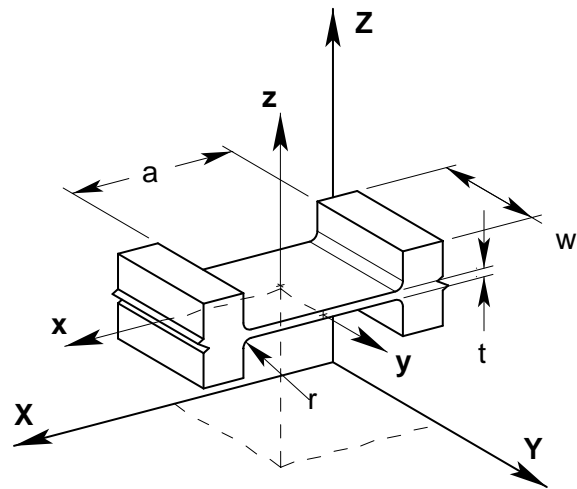
$E := 200000$ Elastic modulus

$\nu := 0.3$ Poisson ratio

$a := 20$

$w := 40$

$t := 0.5$

$k_{act} := 0$

Define below the transformation matrix T(p) for the particular sequence of moves to be used. For each local x-y-z CS, enter values of moves that define it in the corresponding column of the position matrix P below. Include any parameters in the position matrix as desired to aid in changing the configuration.

$$T(p) := R_z(p_6) \cdot T_{xyz}(p_1, p_2, p_3) \cdot R_z(p_5) \cdot R_x(p_4) \qquad\qquad b := 100$$

$$P := \begin{bmatrix} 0 & 0.5 \cdot a & 0 & 0 & 0.5 \cdot a & 0 & 0 & 0.5 \cdot a & 0 \\ b & b + \dfrac{a}{2} & b & b & b + \dfrac{a}{2} & b & b & b + \dfrac{a}{2} & b \\ 0 & 0 & 0 & 0 & 0 & 0 & 0 & 0 & 0 \\ 90 \cdot \deg & 90 \cdot \deg & 0 & 90 \cdot \deg & 90 \cdot \deg & 0 & 90 \cdot \deg & 90 \cdot \deg & 0 \\ 0 & 90 \cdot \deg & 0 & 0 & 90 \cdot \deg & 0 & 0 & 90 \cdot \deg & 0 \\ 240 \cdot \deg & 240 \cdot \deg & 240 \cdot \deg & 0 & 0 & 0 & 120 \cdot \deg & 120 \cdot \deg & 120 \cdot \deg \end{bmatrix}$$

Expressed in the base CS, the rotation matrix transforms either a force-moment vector or a differential displacement-rotation vector in the new CS to the base CS. Being orthonormal, the transposed rotation matrix gives the inverse transformation. The translation matrix is not orthonormal and transforms only a force-moment vector in the new CS to the base CS. The transposed translation matrix transforms only a differential displacement-rotation vector in the base CS to the new CS. The same applies to a general [6 x 6] transformation matrix.

$$
R_x(x) \equiv \begin{bmatrix}
1 & 0 & 0 & 0 & 0 & 0 \\
0 & \cos(x) & -\sin(x) & 0 & 0 & 0 \\
0 & \sin(x) & \cos(x) & 0 & 0 & 0 \\
0 & 0 & 0 & 1 & 0 & 0 \\
0 & 0 & 0 & 0 & \cos(x) & -\sin(x) \\
0 & 0 & 0 & 0 & \sin(x) & \cos(x)
\end{bmatrix}
$$

[6 x 6] rotation matrix for rotation about the x-axis.

$$
R_y(y) \equiv \begin{bmatrix}
\cos(y) & 0 & \sin(y) & 0 & 0 & 0 \\
0 & 1 & 0 & 0 & 0 & 0 \\
-\sin(y) & 0 & \cos(y) & 0 & 0 & 0 \\
0 & 0 & 0 & \cos(y) & 0 & \sin(y) \\
0 & 0 & 0 & 0 & 1 & 0 \\
0 & 0 & 0 & -\sin(y) & 0 & \cos(y)
\end{bmatrix}
$$

[6 x 6] rotation matrix for rotation about the y-axis.

$$
R_z(z) = \begin{bmatrix}
\cos(z) & -\sin(z) & 0 & 0 & 0 & 0 \\
\sin(z) & \cos(z) & 0 & 0 & 0 & 0 \\
0 & 0 & 1 & 0 & 0 & 0 \\
0 & 0 & 0 & \cos(z) & -\sin(z) & 0 \\
0 & 0 & 0 & \sin(z) & \cos(z) & 0 \\
0 & 0 & 0 & 0 & 0 & 1
\end{bmatrix}
$$

[6 x 6] rotation matrix for rotation about the z-axis.

$$
T_{xyz}(x, y, z) \equiv \begin{bmatrix}
1 & 0 & 0 & 0 & 0 & 0 \\
0 & 1 & 0 & 0 & 0 & 0 \\
0 & 0 & 1 & 0 & 0 & 0 \\
0 & -z & y & 1 & 0 & 0 \\
z & 0 & -x & 0 & 1 & 0 \\
-y & x & 0 & 0 & 0 & 1
\end{bmatrix}
$$

[6 x 6] translation matrix for translation in x, y and z.

Define the diagonal elements of the blade's compliance matrix in the local CS.

$$C_{1,1} := \frac{a}{E \cdot t \cdot w} \qquad C_{2,2} := C_{1,1} \cdot \left[\left(\frac{a}{w}\right)^2 + 2.4 \cdot (1 + v) \right] \qquad C_{6,6} := C_{1,1} \cdot \frac{12}{w^2}$$

$$C_{3,3} := C_{1,1} \cdot \left[(1 - v^2) \cdot \left(\frac{a}{t}\right)^2 + 2.4 \cdot (1 + v) \right] \qquad C_{5,5} := C_{1,1} \cdot (1 - v^2) \cdot \frac{12}{t^2}$$

$$C_{4,4} := 12 \cdot \left[\frac{1}{2 \cdot (1 + v)} \cdot \left(4 + 2.52 \cdot \frac{t}{w}\right) \cdot \frac{t^2}{C_{1,1}} + \frac{w^2}{C_{3,3}} \right]^{-1}$$

$$C = \begin{bmatrix} 5 \cdot 10^{-6} & 0 & 0 & 0 & 0 & 0 \\ 0 & 1.69 \cdot 10^{-5} & 0 & 0 & 0 & 0 \\ 0 & 0 & 7.3 \cdot 10^{-3} & 0 & 0 & 0 \\ 0 & 0 & 0 & 4.04 \cdot 10^{-5} & 0 & 0 \\ 0 & 0 & 0 & 0 & 2.18 \cdot 10^{-4} & 0 \\ 0 & 0 & 0 & 0 & 0 & 3.75 \cdot 10^{-8} \end{bmatrix}$$

Define the diagonal elements of the blade's stress matrix in the local CS.

$$S_{1,1} := \frac{1}{t \cdot w} \qquad S_{2,2} := S_{1,1} \cdot \left[\frac{3 \cdot a}{2 \cdot w} + \sqrt{\left(\frac{3 \cdot a}{2 \cdot w}\right)^2 + 1} \right] \qquad S_{6,6} := S_{1,1} \cdot \frac{6}{w}$$

$$S_{3,3} := S_{1,1} \cdot \frac{3 \cdot a}{t} \qquad S_{5,5} := S_{1,1} \cdot \frac{6}{t} \qquad S_{4,4} := S_{3,3} \cdot \frac{6}{w}$$

$$S = \begin{bmatrix} 0.05 & 0 & 0 & 0 & 0 & 0 \\ 0 & 0.1 & 0 & 0 & 0 & 0 \\ 0 & 0 & 6 & 0 & 0 & 0 \\ 0 & 0 & 0 & 0.9 & 0 & 0 \\ 0 & 0 & 0 & 0 & 0.6 & 0 \\ 0 & 0 & 0 & 0 & 0 & 7.5 \cdot 10^{-3} \end{bmatrix}$$

Reflect the compliance and stiffness matrices from the local CS j to the base CS.

$$K_b(j) := T\left(P^{<j>}\right) \cdot C^{-1} \cdot T\left(P^{<j>}\right)^T \qquad\qquad C_b(j) := K_b(j)^{-1}$$

$$K_a(j) := T\left(P^{<j>}\right)^{<1>} \cdot k_{act} \cdot T\left(P^{<j>}\right)^{<1>\,T} \qquad\qquad C_a(j) := K_a(j)^{-1}$$

Combine parallel and series combinations.

$$K_{2\_3} := K_b(2) + K_a(3) \qquad\qquad\qquad C_{2\_3} := K_{2\_3}^{-1}$$

$$K_{5\_6} := K_b(5) + K_a(6) \qquad\qquad\qquad C_{5\_6} := K_{5\_6}^{-1}$$

$$K_{8\_9} := K_b(8) + K_a(9) \qquad\qquad\qquad C_{8\_9} := K_{8\_9}^{-1}$$

$$C_{1\_2\_3} := C_b(1) + C_{2\_3} \qquad\qquad\qquad K_{1\_2\_3} := C_{1\_2\_3}^{-1}$$

$$C_{4\_5\_6} := C_b(4) + C_{5\_6} \qquad\qquad\qquad K_{4\_5\_6} := C_{4\_5\_6}^{-1}$$

$$C_{7\_8\_9} := C_b(7) + C_{8\_9} \qquad\qquad\qquad K_{7\_8\_9} := C_{7\_8\_9}^{-1}$$

$$K_0 := K_{1\_2\_3} + K_{4\_5\_6} + K_{7\_8\_9} \qquad\qquad C_0 := K_0^{-1}$$

$$C_0 = \begin{bmatrix} 3.89 \cdot 10^{-3} & 1.78 \cdot 10^{-15} & 0 & 0 & 0 & 0 \\ 0 & 3.89 \cdot 10^{-3} & 0 & 0 & 0 & 0 \\ 0 & 0 & 1.37 \cdot 10^{-5} & 0 & 0 & 0 \\ 0 & 0 & 0 & 2.72\ 10^{-9} & 0 & 0 \\ 0 & 0 & 0 & 0 & 2.72 \cdot 10^{-9} & 0 \\ 0 & 0 & 0 & 0 & 0 & 3.73\ 10^{-7} \end{bmatrix}$$

$$K_0 = \begin{bmatrix} 256.94 & -1.18\ 10^{-10} & 0 & 1.53\ 10^{-9} & 1.25\ 10^{-9} & 4.66\ 10^{-9} \\ -5.48 \cdot 10^{-11} & 256.94 & 0 & -1.25 \cdot 10^{-9} & 1.53 \cdot 10^{-9} & 3.86 \cdot 10^{-8} \\ 0 & 0 & 7.28\ 10^{4} & -7.73 \cdot 10^{-7} & -6.01\ 10^{-6} & -3.06 \cdot 10^{-9} \\ 1.53 \cdot 10^{-9} & -1.25 \cdot 10^{-9} & -7.72 \cdot 10^{-7} & 3.68 \cdot 10^{8} & 3 \cdot 10^{-4} & 0 \\ 1.25\ 10^{-9} & 1.53\ 10^{-9} & -6.01\ 10^{-6} & 3\ 10^{-4} & 3.68\ 10^{8} & 0 \\ -3.48 \cdot 10^{-9} & 3.56 \cdot 10^{-8} & -3.06 \cdot 10^{-9} & 0 & 0 & 2.68 \cdot 10^{6} \end{bmatrix}$$

6.4.2 Kinematic Coupling Analysis Program

This program helps the user develop a parameterized model of a kinematic coupling so that its ability to reach a seated position may be optimized. The coupling reaches a seated position when all six constraint surfaces are contacting. It approaches the seated position from one of several directions determined by the surfaces already in contact. The limiting case will always occur with five surfaces in contact, and there are only six such directions. The program determines the six directions then solves for the corresponding coefficients of friction that just impede sliding. The smallest coefficient of friction among the six is the limiting coefficient of friction. The program varies parameters between limits set by the user and plots the limiting coefficient of friction. This visual feedback helps the user find the global optimum for this highly coupled, nonlinear problem. In addition, the program calculates the following items for the optimized coupling assuming zero friction: stiffness and compliance matrices, coupling displacement, and contact forces. Due to lengthy calculations, it is advisable to set automatic calculation off.

This program uses six dimensional vectors and [6 x 6] matrices to deal simultaneously with both linear and angular measures. The first three components correspond to linear measures such as force and displacement, and the last three correspond to angular measures such as moment and rotation. The same arrangement applies to the rows and columns of the matrices used for coordinate transformation, stiffness and compliance. In addition, the positions and orientations for six constraint surfaces are conveniently stored in a matrix with six columns. Each column describes a sequence of moves required to go from the global X-Y-Z CS (coordinate system) to a local x-y-z CS as shown in the figure. This matrix also contains the parameters that the program varies in the optimization process. Forces and displacements for the kinematic coupling are represented in the global CS while forces and displacements at a particular constraint are represented in its local x-y-z CS. The z direction represents the outward facing normal of the fixed surface so that a negative displacement is movement of the coupling into contact.

The transformations between the X-Y-Z CS and x-y-z CS's are done as a sequence of moves. The number and order may vary to suit the application, but they must be the same for each constraint since they are stored in a matrix. The basic moves are: translation in x-y-z, rotation about x, rotation about y and rotation about z. The sequence may be interpreted as moves relative to the base CS or in the opposite order as moves relative to the local CS. Two rules express these interpretations for a sequence of transformation matrices: 1) post multiply to transform in the local CS and 2) pre multiply to transform in the base CS. A typical sequence relative to the base CS is: rotate about the X axis, rotate about the Y axis, rotate about the Z axis, and translate (X, Y, Z). The equivalent sequence relative to the local CS is: translate (x, y, z) (initially coincident with the base CS), rotate about the z axis, rotate about the y axis, and rotate about the x axis. The transformation matrix for this sequence is $T_{XYZ} R_Z R_Y R_X$.
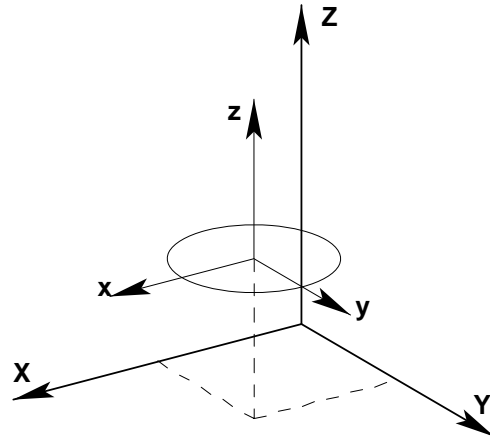
Define below the transformation matrix T(p) for the particular sequence of moves to be used. For each local x-y-z CS, enter values of moves that define it in the corresponding column of the position matrix P(θ) below. Include components of the parameter vector θ in the position matrix to allow optimization of the coupling.

$$T(p) := T_{xyz}(p_1, p_2, p_3) \cdot R_z(p_6) \cdot R_y(p_5) \cdot R_x(p_4)$$

$$P(\theta) := \begin{bmatrix} -0.385 & -0.385 & 0.385 & 0.385 & -0.397 & 0.397 \\ -0.315 & -0.315 & -0.315 & -0.315 & -0.241 & -0.241 \\ -0.8 & -0.8 & -0.8 & -0.8 & 0.85 & 1.31 \\ \theta_2 & -\theta_3 & \theta_2 & -\theta_3 & 90 \cdot deg & 90 \cdot deg \\ -\theta_1 & -\theta_1 & \theta_1 & \theta_1 & 0 & 0 \\ 0 & 0 & 0 & 0 & -\theta_4 & \theta_4 \end{bmatrix}$$

Enter a vector k of contact stiffnesses and a vector f of forces and moments applied to the coupling at the origin of X-Y-Z. Note, a transformation matrix may be used to apply the force elsewhere.

$$k := \begin{bmatrix} 1 \\ 1 \\ 1 \\ 1 \\ 1 \\ 1 \end{bmatrix} \qquad f := \begin{bmatrix} 0 \\ 0 \\ -450 \\ 0 \\ 0 \\ 0 \end{bmatrix}$$

Expressed in the base CS, the rotation matrix transforms either a force-moment vector or a differential displacement-rotation vector in the new CS to the base CS. Being orthonormal, the transposed rotation matrix gives the inverse transformation. The translation matrix is not orthonormal and transforms only a force-moment vector in the new CS to the base CS. The transposed translation matrix transforms only a differential displacement-rotation vector in the base CS to the new CS. The same applies to a general [6 x 6] transformation matrix.

$$R_x(x) \equiv \begin{bmatrix} 1 & 0 & 0 & 0 & 0 & 0 \\ 0 & \cos(x) & -\sin(x) & 0 & 0 & 0 \\ 0 & \sin(x) & \cos(x) & 0 & 0 & 0 \\ 0 & 0 & 0 & 1 & 0 & 0 \\ 0 & 0 & 0 & 0 & \cos(x) & -\sin(x) \\ 0 & 0 & 0 & 0 & \sin(x) & \cos(x) \end{bmatrix}$$

[6 x 6] rotation matrix for rotation about the x-axis.

$$R_y(y) \equiv \begin{bmatrix} \cos(y) & 0 & \sin(y) & 0 & 0 & 0 \\ 0 & 1 & 0 & 0 & 0 & 0 \\ -\sin(y) & 0 & \cos(y) & 0 & 0 & 0 \\ 0 & 0 & 0 & \cos(y) & 0 & \sin(y) \\ 0 & 0 & 0 & 0 & 1 & 0 \\ 0 & 0 & 0 & -\sin(y) & 0 & \cos(y) \end{bmatrix}$$

[6 x 6] rotation matrix for rotation about the y-axis.

$$R_z(z) \equiv \begin{bmatrix} \cos(z) & -\sin(z) & 0 & 0 & 0 & 0 \\ \sin(z) & \cos(z) & 0 & 0 & 0 & 0 \\ 0 & 0 & 1 & 0 & 0 & 0 \\ 0 & 0 & 0 & \cos(z) & -\sin(z) & 0 \\ 0 & 0 & 0 & \sin(z) & \cos(z) & 0 \\ 0 & 0 & 0 & 0 & 0 & 1 \end{bmatrix}$$

[6 x 6] rotation matrix for rotation about the z-axis.

$$T_{xyz}(x,y,z) \equiv \begin{bmatrix} 1 & 0 & 0 & 0 & 0 & 0 \\ 0 & 1 & 0 & 0 & 0 & 0 \\ 0 & 0 & 1 & 0 & 0 & 0 \\ 0 & -z & y & 1 & 0 & 0 \\ z & 0 & -x & 0 & 1 & 0 \\ -y & x & 0 & 0 & 0 & 1 \end{bmatrix}$$

[6 x 6] translation matrix for translation in x, y and z.

A coupling with only five surfaces in contact is free to slide in one direction. In this direction, the stiffness matrix is singular, assuming zero friction. The eigenvector of the stiffness matrix corresponding to the zero eigenvalue provides the direction of sliding, although it may have the wrong sign. The stiffness matrix K for the coupling is a summation of contact stiffnesses transformed to the global CS. The definition of K below excludes the jth contact surface from the sum. Use j = 0 to calculate K with all surfaces in contact. The matrix Δ contains the six sliding directions in its columns, all relative to the global CS.

$$K(P,j) := \sum_{i=1}^{6} T\left(P^{<i>}\right)^{<3>} \cdot k_i \cdot (i \neq j) \cdot T\left(P^{<i>}\right)^{<3>^T}$$

$$\Delta(P) := \begin{vmatrix} \text{for} & i \in 1..6 \\ \quad \Delta^{<i>} \leftarrow \text{eigenvec}(K(P,i),0) \\ \Delta \end{vmatrix}$$

The coefficient of friction that just impedes sliding causes the coupling to be in static equilibrium. Obviously the non contacting surface has zero normal force. Therefore, static equilibrium equations can be solved to determine the coefficient of friction that makes the normal force zero at the surface intended to be noncontacting. This first requires a relationship for the friction force. Given a sliding direction δ and a coefficient of friction μ, the vector ϕ is a normalized force-moment vector that includes tangential friction. Both δ and ϕ are defined in the local x-y-z CS. Transformed to the global CS, ϕ's for all six contact surfaces are assembled in matrix A. Matrix A multiplied by a six-component vector of surface normal forces equals the resultant force-moment vector for the coupling.

$$\phi(\delta,\mu) := \left[\frac{-\mu \cdot \delta_1}{\left|\left[\delta_1 \quad \delta_2 \quad \delta_3\right]^T\right|} \quad \frac{-\mu \cdot \delta_2}{\left|\left[\delta_1 \quad \delta_2 \quad \delta_3\right]^T\right|} \quad 1 \quad 0 \quad 0 \quad 0 \right]^T$$

$$A(P, \delta, \mu) := \begin{vmatrix} \text{for} \quad i \in 1..6 \\ \qquad A^{<i>} \leftarrow T(P^{<i>}) \cdot \phi\left(T(P^{<i>})^T \cdot \delta, \mu\right) \\ A \end{vmatrix}$$

Since matrix A is invertible, the surface normal forces are linearly solved from the applied force-moment vector f. The only one of interest is the surface intended to be non contacting, which is zero at equilibrium. The root of this nonlinear equation provides the coefficient of friction that just impedes sliding. The coefficients of friction for all six sliding directions are assembled in vector μ.

$\mu := 0$ Starting value for the solver.

$$\mu(P, \Delta) := \begin{vmatrix} \text{for} \quad i \in 1..6 \\ \qquad \mu_i \leftarrow \left| \text{root}\left(\text{lsolve}\left(A\left(P, \Delta^{<i>}, \mu\right), f\right)_i, \mu\right) \right| \\ \mu \end{vmatrix}$$

he program plots curves of the limiting coefficient of friction over ranges of parameters that vary
ndividually. Each curve is a function of one parameter while the others are held at nominal values. The
ser will adjust the nominal set towards the optimal set. Enter minimum and maximum values for the
arameter ranges to plot. Enter the nominal parameter set. Enter the number of points to plot over the
ange (typically $n_r := 5$). Enter the number of parameters (typically $n_p := \text{rows}(\theta)$ but may be fewer).
tart the calculation (command =) if in manual mode.

$$\theta_{min} := \begin{bmatrix} 35 \\ 15 \\ 30 \\ 45 \end{bmatrix} \cdot \deg \qquad \theta_{max} := \begin{bmatrix} 55 \\ 35 \\ 50 \\ 65 \end{bmatrix} \cdot \deg \qquad \theta := \begin{bmatrix} 40 \\ 25 \\ 45 \\ 60 \end{bmatrix} \cdot \deg \qquad \overrightarrow{\frac{\theta - \theta_{min}}{\theta_{max} - \theta_{min}}} = \begin{bmatrix} 0.25 \\ 0.5 \\ 0.75 \\ 0.75 \end{bmatrix}$$

$n_r := 5$ $i := 1..n_r$ $P_\theta := P(\theta)$

$n_p := 4$ $j := 1..n_p$ $\text{rank}(K(P_\theta, 0)) = 6$

$\alpha_i := \dfrac{i - 1}{n_r - 1}$

$$\theta_r(i, j) := \begin{vmatrix} \theta_r \leftarrow \theta \\ \theta_{r_j} \leftarrow (1 - \alpha_i) \cdot \theta_{min_j} + \alpha_i \cdot \theta_{max_j} \\ \theta_r \end{vmatrix}$$

$\mu_\theta := \mu(P_\theta, \Delta(P_\theta))$

$$\mu_\theta = \begin{bmatrix} 0.391 \\ 0.445 \\ 0.53 \\ 0.441 \\ 0.378 \\ 0.387 \end{bmatrix}$$

$$\mu_{r_{i, j}} := \min\left(\mu\left(P\left(\theta_r(i, j)\right), \Delta\left(P\left(\theta_r(i, j)\right)\right)\right)\right)$$

f necessary, change the number of curves to match the number of parameters. Since the
arameters may vary over different ranges, it is convenient to plot the curves over a normalized
ange between 0 and 1. The horizontal dashed line is the limiting coefficient of friction for the
ominal parameter set. It crosses each curve at the nominal parameter value. The goal is to adjust
he nominal set so that the horizontal line crosses near the peaks of the curves. Another indication
f being near the optimum is a good balance among components in μ_θ, the coefficients of friction
or the six sliding directions.

$$\theta^T = \begin{bmatrix} 40 & 25 & 45 & 60 \end{bmatrix} \cdot \deg$$
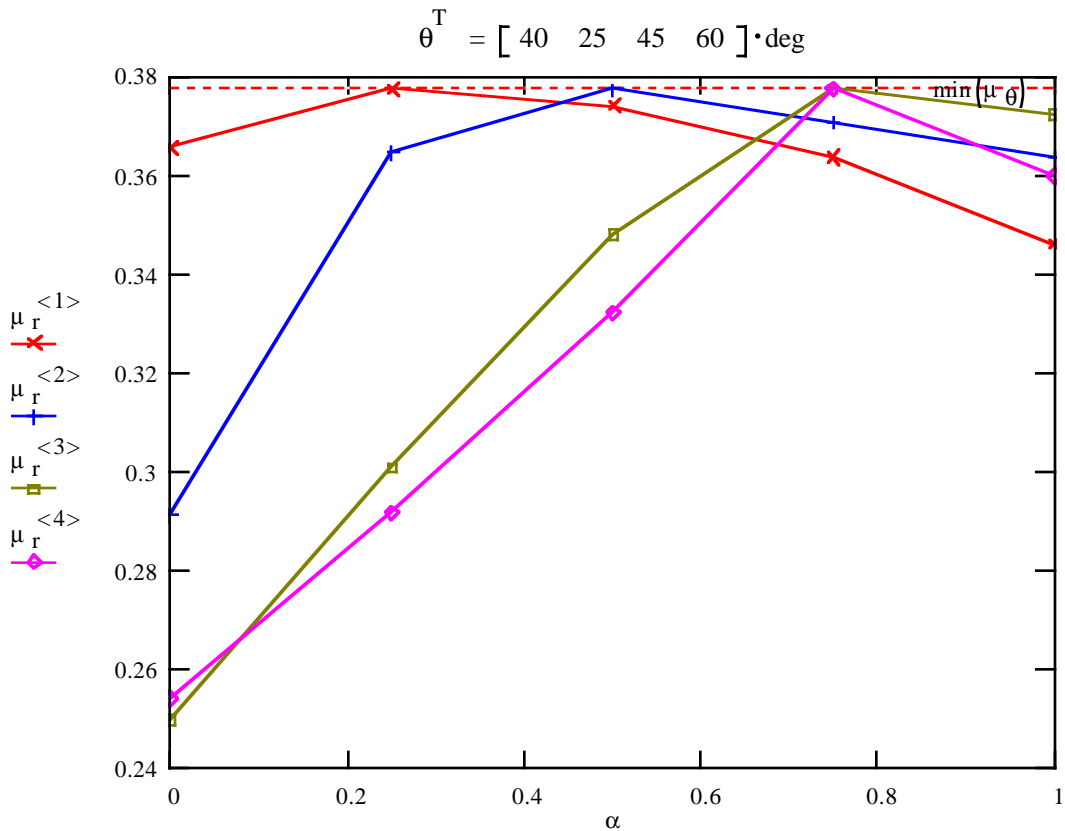
Display the optimized position matrix of constraints $P(\theta)$, the sliding directions $\Delta(P)$
and the corresponding coefficients of friction μ_θ. Each column corresponds to a
particular constraint.

$$P_\theta = \begin{bmatrix} -0.385 & -0.385 & 0.385 & 0.385 & -0.397 & 0.397 \\ -0.315 & -0.315 & -0.315 & -0.315 & -0.241 & -0.241 \\ -0.8 & -0.8 & -0.8 & -0.8 & 0.85 & 1.31 \\ 0.436 & -0.785 & 0.436 & -0.785 & 1.571 & 1.571 \\ -0.698 & -0.698 & 0.698 & 0.698 & 0 & 0 \\ 0 & 0 & 0 & 0 & -1.047 & 1.047 \end{bmatrix}$$

$$\Delta\left(P_{\theta}\right) = \begin{bmatrix} -0.322 & 7.232 \cdot 10^{-3} & -0.341 & -0.034 & 0.392 & 0.378 \\ -0.121 & 0.2 & 0.222 & 0.203 & 0.525 & -0.531 \\ 0.325 & 0.276 & -0.361 & 0.275 & -0.207 & 0.209 \\ -0.229 & 0.193 & 0.097 & 0.189 & -0.656 & 0.664 \\ 0.318 & -0.02 & 0.295 & -1.307 \cdot 10^{-3} & 0.311 & 0.3 \\ 0.789 & -0.92 & 0.779 & 0.92 & 0 & 0 \end{bmatrix}$$

$$\mu_{\theta}^{\ T} = \begin{bmatrix} 0.391 & 0.445 & 0.53 & 0.441 & 0.378 & 0.387 \end{bmatrix}$$

Display a vector of surface normal forces, the couplings displacement, and the stiffness and compliance matrices.

$$f_{norm} := \text{lsolve}\left(A\left(P_{\theta}, 0, 0\right), f\right) \qquad K_{\theta} := K\left(P_{\theta}, 0\right) \qquad C_{\theta} := K_{\theta}^{-1}$$

$$f_{norm}^{\ T} = \begin{bmatrix} -180.844 & -169.289 & -203.765 & -168.51 & -83.822 & -68.812 \end{bmatrix} \qquad C_{\theta} \cdot f = \begin{bmatrix} 1.809 \\ 57.505 \\ -317.867 \\ -94.622 \\ 17.728 \\ 23.375 \end{bmatrix}$$

$$K_{\theta} = \begin{bmatrix} 2.592 & 0 & 0 & 0.199 & 0.245 & 0.42 \\ 0 & 1.857 & 0.179 & 0.489 & -0.199 & 0 \\ 0 & 0.179 & 1.551 & -0.345 & 0 & 0 \\ 0.199 & 0.489 & -0.345 & 1.542 & 0.43 & 2.349 \cdot 10^{-3} \\ 0.245 & -0.199 & 0 & 0.43 & 3.559 & -0.487 \\ 0.42 & 0 & 0 & 2.349 \cdot 10^{-3} & -0.487 & 0.346 \end{bmatrix}$$

$$C_{\theta} = \begin{bmatrix} 0.544 & -0.01 & -4.02 \cdot 10^{-3} & -0.023 & -0.155 & -0.878 \\ -0.01 & 0.625 & -0.128 & -0.249 & 0.084 & 0.132 \\ -4.02 \cdot 10^{-3} & -0.128 & 0.706 & 0.21 & -0.039 & -0.052 \\ -0.023 & -0.249 & 0.21 & 0.815 & -0.133 & -0.165 \\ -0.155 & 0.084 & -0.039 & -0.133 & 0.419 & 0.778 \\ -0.878 & 0.132 & -0.052 & -0.165 & 0.778 & 5.048 \end{bmatrix}$$